

THE CHARACTERIZATION AND EVALUATION OF A SEALED CELL MERCURY
RESONANCE IONIZATION IMAGING DETECTOR

By

MICHAEL RODNEY SHEPARD

A DISSERTATION PRESENTED TO THE GRADUATE SCHOOL
OF THE UNIVERSITY OF FLORIDA IN PARTIAL FULFILLMENT
OF THE REQUIREMENTS FOR THE DEGREE OF
DOCTOR OF PHILOSOPHY

UNIVERSITY OF FLORIDA

2002

This dissertation is dedicated to the memory of my grandfather and best friend, Dean Clay Greer, and to the memory of my grandfather and mentor, John Shepard.

ACKNOWLEDGMENTS

In the years since I first came to the University of Florida I have overcome many of, perhaps, my life's greatest trials. More recently, I have been blessed with the arrival of a healthy and beautiful daughter, Hannah Grace Shepard. And now, as I approach the end of my graduate career, I can fully realize and appreciate all these personal and professional experiences.

My success as a graduate student is to be attributed to all of those who have helped me along the way. With that said, my foremost thanks go to my research advisor, Dr. James Winefordner. His knowledge of the field and passion to teach provided a wonderful learning environment. His flexibility and sense of humor created a pleasurable work place. Finally, it was his sincerity and patience on those "rainy days" that made this degree attainable for me.

Gratitude must also go to Dr. Benjamin Smith for his support. Ben's willingness to find the missing power supply or to diagnose an instrumental problem made him an essential resource. His positive attitude and encouraging words of wisdom make him an invaluable friend.

Further gratitude is extended to Dr. Oleg Matveev for his numerous ideas and support of my research progress. Oleg helped to make sense of strange results and always knew of an alternative way make a certain measurement.

I would also like to thank Drs. Kathryn Williams, Robert Kennedy, Weihong Tan, Vaneica Young and Gardiner Myers for their support and direction during my teaching appointments. I am also grateful to the US Defense Advanced Research Projects Agency, the US National Institute of Health (Grant HL63965), the Graduate Student Counsel, and Dr. John Helling for funding support of my research and travel.

My greatest support over the past five years has undoubtedly come from my wife, Michele. It is for that reason that I give my deepest thanks to her. Without her support and encouragement, I would not have found the motivation to complete this work.

Finally, I would like to extend my gratitude to all the past and present JDW group members that I have worked with for their support and guidance. Special thanks go to those that I worked most closely with, including Jamshid Temirov and Drs. Ricardo Aucélio and Gabor Galbacs.

Above all, I give thanks to God for all of the blessings in my life.

TABLE OF CONTENTS

	<u>page</u>
ACKNOWLEDGMENTS	iii
LIST OF TABLES	vii
LIST OF FIGURES	viii
ABSTRACT.....	x
CHAPTERS	
1 THE GOAL OF THE PROJECT	1
2 INTRODUCTION TO RESONANCE IONIZATION IMAGING DETECTORS.....	3
Background	3
Historical Preface to Resonance Ionization Spectroscopy.....	3
Ultra-narrowband Imaging Detectors	5
Luminosity-Resolving Power Product.....	8
Principles of Operation	9
Modes of Operation	12
Detection of Charged Particles.....	12
Signal measurement	14
Experimental Description	16
Previous Resonance Ionization Imaging Detectors	20
3 EVALUATION AND CHARACTERIZATION OF THE RIID	26
Sources of Noise	26
Spectral Bandwidth and Range	27
Sensitivity.....	33
Spatial Resolution	33
Temporal Resolution and Response.....	34
Quantum Efficiency	36

4	TIME RESOLVED MEASUREMENTS IN THE RIID	38
	Photoelectric effect in the RIID	38
	Temporal Response of the RIID in Non-imaging Mode	39
	Effect of λ_2 and λ_3 Position within the RIID.....	39
	Effect of High Voltage Application	43
	Signal-to-Noise Ratio in Non-imaging Mode	45
	Unidentified Ionization Component	47
5	IMAGE DISTORTIONS IN THE RIID	54
	Overview of Image Distortions.....	54
	Experimental	56
	Temporal Distortions	56
	Spatial Distortions.....	64
6	POTENTIAL APPLICATIONS	67
	Moving Object Detection.....	67
	Monte Carlo Simulation of Moving Object Detection.....	69
7	FINAL COMMENTS	83
	Conclusions.....	83
	Future Work.....	83
	LIST OF REFERENCES	85
	BIOGRAPHICAL SKETCH	90

LIST OF TABLES

<u>Table</u>	<u>page</u>
2-1. Elements suitable for use in UBID systems.	7
3-1. List of elements suitable for use as the RIID's active medium.	32
6-1. MCS software variable definitions and default values.	70

LIST OF FIGURES

<u>Figure</u>	<u>page</u>
2-1. Schematic representation of several atomic vapor ultra-narrowband imaging detectors.	4
2-2. Luminosity-resolving power product (adapted from Matveev <i>et al.</i>) for several spectroscopic systems.	10
2-3. Two and three color ionization schemes for mercury.	11
2-4. Side view illustration of the RIID for imaging mode operation. λ_2 and λ_3 are perpendicular with λ_1 and the place of the paper.....	13
2-5. Side view illustration of the RIID for non-imaging mode operation. λ_2 and λ_3 are perpendicular with λ_1 and the place of the paper.....	15
2-6. The sealed-cell mercury resonance ionization imaging detector.....	18
2-7. High voltage divider for the RIID.	19
2-8. Experimental setup of the RIID.....	21
2-9. Image quality versus high voltage across the voltage divider.....	22
2-10. Imaging mask.	23
2-11. Prototype RIID with MCP.....	25
3-1. Spectral response of the RIID in non-imaging mode as λ_1 is detuned away from the center of resonance line.....	29
3-2. Isotope and hyperfine splitting of mercury's ground state transition ($6^1S_0 \rightarrow 6^3P_1$) (adapted from Grossman <i>et al.</i>)	30
3-3. RIID captured image with 80 μm spatial resolution.	35
4-1. Time resolved measurement in the RIID.....	40
4-2. RIID schematic showing λ_2 and λ_3 position and signal generation.	41

4-3.	Non-imaging mode signal when the ionization region shifted away from input window toward the MCP.	42
4-4.	Imaging mode detection for λ_2 and λ_3 close to input window and MCP.	44
4-5.	Effect of high voltage upon non-imaging mode signal.	46
4-6.	Non-imaging mode signal-to-noise ratio of 135 for $V = 9.0\text{kV}$ and 10^9 incident photons. (—) shows noise due to λ_2 and λ_3 beams only; (—) shows signal when all three beams are present.	48
4-7.	Non-imaging mode signal-to-noise ratio of 64 for $V = 9.5\text{kV}$ and 10^5 incident photons.	49
4-8.	Peak separation as a function of $V_{\text{MCP-IW}}$	51
4-9.	Peak intensity ratio as a function of $V_{\text{MCP-IW}}$	52
5-1.	Image series with $V_{\text{MCP-IW}} = 4.8\text{kV}$	57
5-2.	Image series with $V_{\text{MCP-IW}} = 1.0\text{kV}$	60
5-3.	Spatial Resolution as a function of time. • - $V_{\text{MCP-IW}} = 4.8\text{ kV}$; Δ - $V_{\text{MCP-IW}} = 1.0\text{ kV}$	61
5-4.	Signal conservation during image distortions.	63
5-5.	Spatial image distortions in the RIID.	65
6-2.	Schematic diagram of MCS model.	71
6-3.	Simulation with $V_{\text{disk}} = 0\text{ m/s}$ and $v_{\text{center}} = 0$	73
6-4.	Simulation with $V_{\text{disk}} = 30.0\text{m/s}$ and $v_{\text{center}} = 0$	75
6-5.	Simulation with $V_{\text{disk}} = 30.0\text{m/s}$ and $v_{\text{center}} = 2580 \times 10^{-6}\text{ cm}^{-1}$	76
6-6.	Doppler shifted profiles.	78
6-7.	Simulation with $V_{\text{disk}} = 30.0\text{m/s}$, $v_{\text{center}} = 2580 \times 10^{-6}\text{ cm}^{-1}$, and $\mu_{\text{scat}} = 32.0\text{ mm}^{-1}$	79
6-8.	Simulation with $V_{\text{disk}} = 30.0\text{m/s}$, $v_{\text{center}} = 2580 \times 10^{-6}\text{ cm}^{-1}$, $\mu_{\text{scat}} = \mu_{\text{scat}} = 12.0\text{ mm}^{-1}$	81

Abstract of Dissertation Presented to the Graduate School
of the University of Florida in Partial Fulfillment of the
Requirements for the Degree of Doctor of Philosophy

THE CHARACTERIZATION AND EVALUATION OF A SEALED CELL MERCURY
RESONANCE IONIZATION IMAGING DETECTOR

By

Michael Rodney Shepard

August 2002

Chair: James D. Winefordner
Department: Chemistry

In many fields of imaging science, there is an increasing demand for detectors with high sensitivity as well as high spatial, spectral, and temporal resolution. Although conventional imaging systems frequently excel in one of these aspects, it is often at the expense of the others. The mercury vapor filled Resonance Ionization Imaging Detector (RIID) presented here is not subject to this tradeoff. When operated in conjunction with modern narrowband lasers, the analytical figures of merit of the RIID can far exceed those of conventional imaging systems. Under certain operating conditions, the spectral resolution of the RIID can approach the natural atomic linewidth of the contained atomic vapor. This type of ultra-narrowband detector has the potential for a wide range of applications such as the detection of moving objects, the imaging of ultrasonic fields, plasma diagnostics, and high-energy particle detection, among others. Additionally, the RIID can be operated in a variety of modes providing multifaceted system information.

A compact, sealed cell version of a mercury vapor RIID is demonstrated in this study. The figures of merit obtainable with this novel design are presented. The signal-to-noise ratio of the RIID in ion detection mode for both imaging and non-imaging cases was evaluated. Additionally, the temporal response of the RIID for both imaging and non-imaging modes was studied.

A limitation of the compact mercury RIID is realized in the imaging mode. The operating conditions for optimal image signal-to-noise and spatial resolution in the RIID were shown to result in severe image distortions. Several methods for relieving such distortions are proposed.

CHAPTER 1 THE GOAL OF THE PROJECT

In many fields of imaging science, there is an increasing demand for optical detectors with improved imaging figures of merit. The resonance ionization imaging detector (RIID) has potential applications in many of these fields and can offer improved spectral resolution and sensitivity with comparable spatial and temporal resolution. It has been suggested that the RIID could be used in a variety of applications ranging from ultrasonic field detection and chemical Raman Imaging to atmospheric projectile and satellite tracking [1]. The potential for this type of ultra-narrowband imaging detector has not yet been fully realized, nor has the technology been fully developed.

The prototype RIID, experimentally demonstrated at the University of Florida in 1998, featured a low pressure mercury vapor imaging cell [2,3]. This prototype ionization imaging detector successfully demonstrated the sensitivity and selectivity of atomic vapor, ultra-narrowband detection principles. Additionally, it was shown that 2-dimensional (2-D) imaging information was obtainable with this type of detector [4]. However, the experimental design of this prototype RIID featured a series of vacuum pumps, a large atom reservoir, and an intensified charge coupled device (CCD) detector among a host of other bulky components. The colossal design of this prototype was not practical for the applications in imaging science as discussed above. In addition to these spatial constraints, other aspects of the prototype design limit the application of the detector. The cumbersome nature of turbomolecular vacuum pump system, the external

atom reservoir, and the complex optical design of the system were all undesirable features of this initial design.

The goal of this work was to characterize and evaluate the performance of a compact variant of the mercury resonance ionization imaging detector. A cell was designed and manufactured to contain all of the necessary components of the RIID into a sealed and compact detector. The performance of this RIID was evaluated using two separate ionization schemes for comparison. Both schemes were based upon the ground state absorption of 254 nm photons. The behavior of the RIID for both imaging and non-imaging modes of detection was investigated. The RIID was also studied for both ion and electron detection modes.

CHAPTER 2 INTRODUCTION TO RESONANCE IONIZATION IMAGING DETECTORS

Increasing demands in imaging science have brought forth the development of spectrally selective, atomic vapor imaging detectors and filters [5-7]. The photon detector evaluated in this work unites the well-established principles of resonance ionization spectroscopy with modern imaging science and related fields.

Background

A new generation of ultra-narrowband imaging detectors (UBIDs) can offer spectral resolutions limited only by the natural atomic linewidth of the contained atomic vapor. Compared to conventional imaging techniques, the use of UBIDs can result in a resolution improvement of 2-4 orders of magnitude [1,8,9]. Figure 2-1 illustrates three types of UBIDs and the respective instrument function of each. Additionally, UBIDs demonstrate the ability to detect low signal levels in the presence of a high background. One such UBID, the resonance ionization imaging detector (RIID), can provide a spectral resolution on the order of 1.4 MHz when an atomic mercury vapor is used as the medium [10].

Applications which may require this type of high spectral resolution and sensitivity include laser Doppler velocimetry, ultrasonic field imaging, and moving object detection. Potential applications of the RIID will be discussed later in this dissertation.

Historical Preface to Resonance Ionization Spectroscopy

Resonance ionization spectroscopy (RIS) was first proposed in the early 1970s by Letokhov for isotopic speciation and trace metal detection [11]. The first experimental

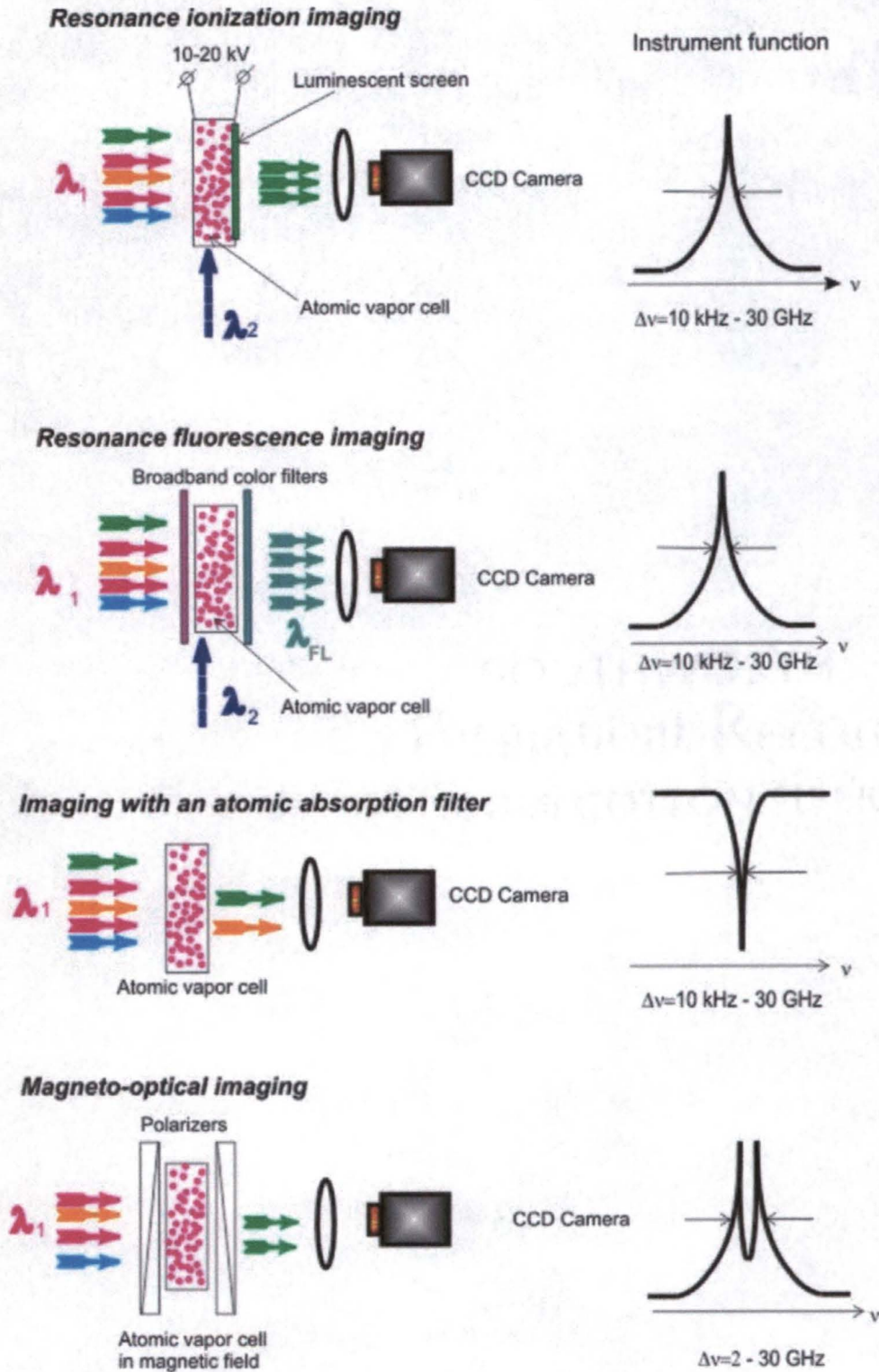


Figure 2-1. Schematic representation of several atomic vapor ultra-narrowband imaging detectors.

demonstration of RIS was performed in 1971 at the Institute of Spectroscopy of the USSR Academy of Sciences [11-13]. This experiment featured a 2 step photoionization scheme for rubidium atoms. A tunable dye laser, pumped by a Ruby laser, was used to first excite the ground state Rb atoms into the $5^2P_{1/2}$ state. The second-harmonic output pulses of the Ruby laser were then sufficient to photoionize the excited state Rb atoms. The selectivity of this scheme was demonstrated as the energy of the second-harmonic output pulses of the Ruby laser were insufficient to photoionize the ground state Rb atoms. The authors cited an overall ionization efficiency of about 0.1%.

By 1977, the success of this newfound ionization technique brought forth the first analytical experiments for detection of single atoms [11]. Hurst *et al.*, at Oak Ridge National Laboratory, used a two-step photoionization scheme for the detection of single cesium atoms in a buffer gas [11,14-15].

Since these first experiments, resonance ionization schemes and supporting experiments have been reported for atoms of nearly every element [11,15-18]. The underlying principles of RIS have been applied to molecular methods for improved selectivity as well [11,14]. Most notable is the coupling of RIS with mass spectrometry for techniques such as resonance enhanced multiphoton ionization mass spectrometry (REMPI-MS) and resonance ionizing mass spectrometry (RIMS) [19-22]. The principles of RIS are applied in this work, not for the optical detection of Hg atoms but for the detection of photons by a Hg vapor.

Ultra-narrowband Imaging Detectors

Atomic vapors have very narrow absorption lines making them ideal candidates for use as narrowband optical filters or as active media in UBIDs. When monoisotopic atomic vapors are used, or when Doppler-free techniques are employed, the spectral

response of the detector or filter is further improved. In the case of a mercury vapor UBID, the spectral resolution can be improved from over 1.0 GHz to 1.45 MHz. The spectral resolution of conventional imaging systems is at best 20-50 GHz [1]. Only photons, whose frequency falls within this exceptionally narrow linewidth, will be absorbed by the contained atomic vapor for eventual detection. The inherent selectivity and spectral resolution of UBIDs arise from this fact. Selectivity is further added to this mode of photon detection when additional transitions are utilized for detection as is the case with the RIID and resonance fluorescence imaging monochromator (RFIM). Such atomic vapor imaging detectors have limited spectral ranges corresponding to the absorption frequencies of a few volatile elements. The availability of laser systems further limits the application of this technology. At present, there are at least 23 elements that are suitable for use in most UBID systems including Cs, Hg, Rb, and Sr [1,5,11]. These elements are shown in table 2-1. In the case of the mercury RIID, the high sensitivity results from the final ionization step and by the amplification factor of the microchannel plate (MCP) [23].

In 1996, Matveev *et al.* demonstrated single photo-electron and photon detection using a non-imaging mercury resonance ionization detector (RID) [23]. The RID cell was developed to detect low photon levels following the avalanche ionization of a buffer gas contained within the mercury cell. A limit of detection of 253.7 nm photons, corresponding to the $6^1S_0 \rightarrow 6^3P_1$ transition, was shown to be 0.5 quanta during the lifetime of the excited state.

A naturally occurring mercury vapor was chosen in this work to be the active medium of the RIID for several reasons. The vapor pressure of mercury provides a saturated

Element	Minimal Cell Temperature (°C)
Hg	-59
Cs	0
Rb	17
K	42
Cd	94
Na	99
Zn	148
Mg	207
Yb	231
Li	271
Sr	275
Ca	319
Eu	231
Tl	335
Ba	353
Pb	383
Sm	413
Tm	491
He	N/A
Ne	N/A
Ar	N/A
Kr	N/A
Xe	N/A

Table 2-1. Elements suitable for use in UBID systems.

atomic cell at room temperature (4×10^{13} atoms·cm⁻³). The concentration of gaseous mercury atoms would be sufficient to absorb more than 90% of the resonant photons within an optical path length of 2-3 cm [24]. Additionally, the ultraviolet and visible wavelength transitions are easily obtainable with current lasers systems in our laboratories.

Luminosity-Resolving Power Product

Conventional imaging systems frequently excel in one aspect of image acquisition, while suffering at others [25,26]. The RIID, and UBIDs in general, are not subject to this tradeoff. A figure of merit which best represents the performance of spectroscopic imaging systems is the luminosity-resolving power (LR) product, otherwise known as the spectral efficiency of the imaging system. Resolving powers (R) on the order of 10^6 are achievable for almost all conventional spectroscopic imaging devices. However, the throughput of the device, or luminosity (L) (cm²·sr), is inherently decreased in order to achieve these high resolving powers. For this reason, the product of the luminosity and resolving power (LR) provides more information about a system than does each figure of merit reported separately. The relationship between LR and the signal-to noise ratio (S/N) is also beneficial when evaluating spectroscopic imaging systems. Matveev *et al.* derived an equation relating these figures of merit [25]. This relationship is given in equation 2-1.

$$S/N = \sqrt{LR} \sqrt{\frac{S_0}{B_{\lambda B} \beta \lambda}} \frac{\sqrt{P \epsilon}}{p} \int_0^{\infty} B_{\lambda S}(\lambda) S_n(\lambda) d\lambda \quad (2-1)$$

S_0 is the maximum value of the spectral-detection function, $B_{\lambda B}$ (photons $s^{-1}\cdot sr^{-1}\cdot nm^{-1}$) is the background level, β is a optimal resolution proportionality constant, $\bar{\lambda}$ (nm) is the mean wavelength of incident photons, P is the number of pixels, ϵ is the ratio of the image detector's working area to the total area, p is the effective number of pixels ($P \gg p$), $B_{\lambda S}(\lambda)$ (photons $s^{-1}\cdot sr^{-1}\cdot nm^{-1}$) is source spectral radiance, and $S_n(\lambda)$ (nm) is the normalized spectral-detection function. The LR product for several imaging systems has been evaluated by Matveev *et al.* [26]. Figure 2-2 compares the LR product for many conventional imaging systems with the RIID. As shown, the RIID has a much greater LR product compared to popular imaging systems.

Principles of Operation

The principles of operation for the resonance ionization imaging detector studied here are based upon the resonant photoionization of a isotopic mixture of mercury atoms. In this work, three-step ionization schemes (two or three color) were used where the final transition was non-resonant photoionization. The two schemes employed are shown in figure 2-3. The analytical beam, or probe beam, to be imaged was the first UV transition, denoted λ_1 . This beam is directed through the input (front) window (IW). The absorption of λ_1 (253.7nm) is a resonant transition from the 6^1S_0 ground state to the 6^3P_1 excited state. From the 6^3P_1 level, a second resonant photon (λ_2) at 313.2 nm ($6^3P_1 \rightarrow 6^3D_1$) or 435.8 nm ($6^3P_1 \rightarrow 7^3S_1$) was introduced through the side window. From this point, photoionization was achieved by a third photon ($\lambda_3 = 626.4$ nm, $6^3D_1 \rightarrow Hg^+$; $\lambda_3 = 435.8$ nm, $7^3S_1 \rightarrow Hg^+$) non-resonant transition via the side window.

Upon ionization, the electron/ion pair experience a high electric field (externally applied potential) and are accelerated toward opposite ends of the cell. The polarity of

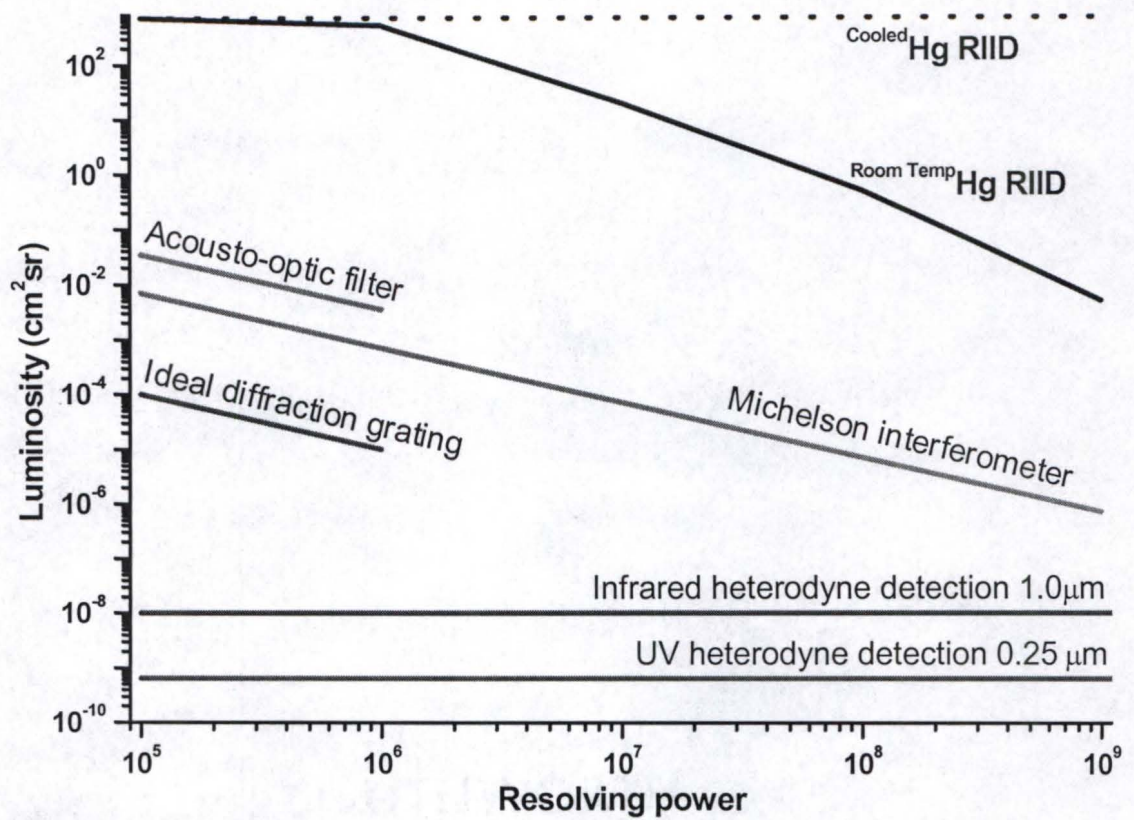


Figure 2-2. Luminosity-resolving power product (adapted from Matveev *et al.*) for several spectroscopic systems [25].

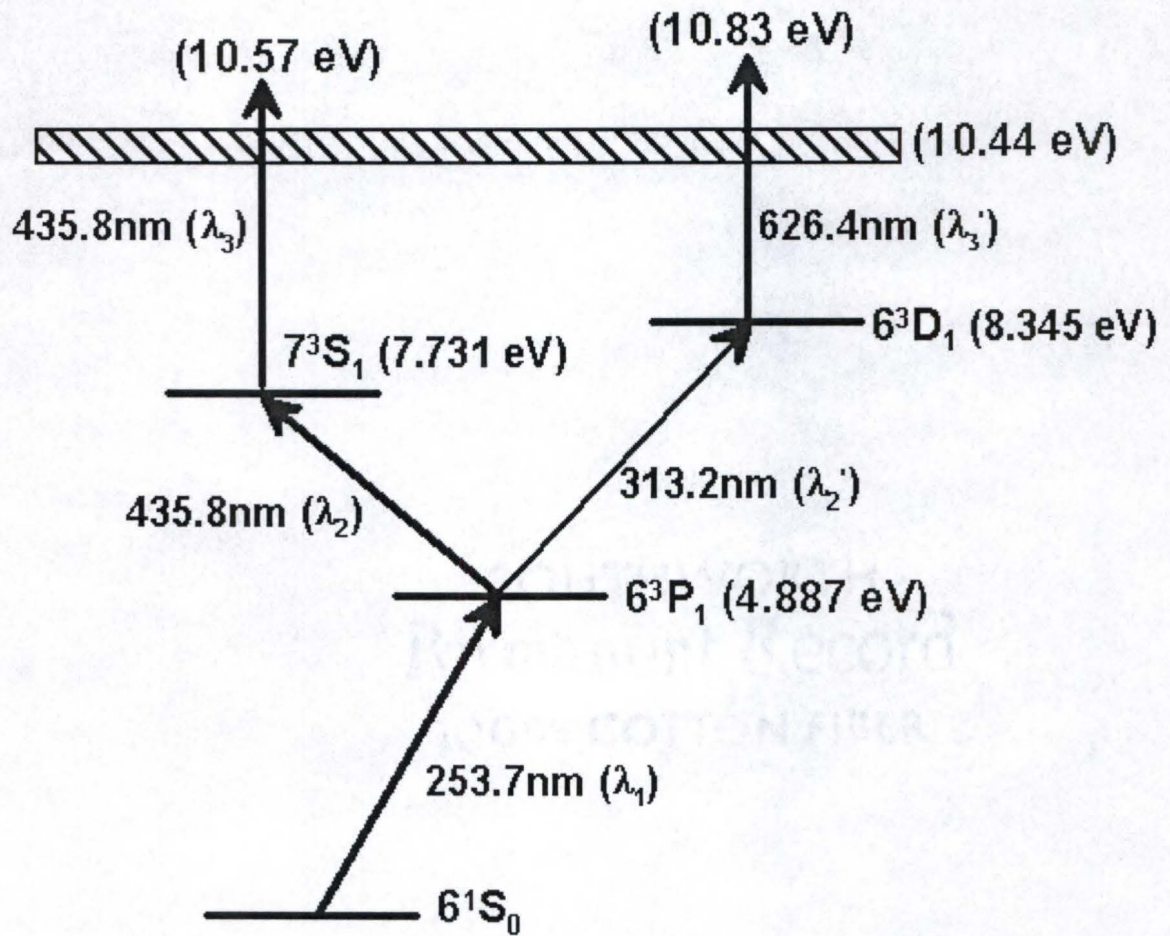


Figure 2-3. Two and three color ionization schemes for mercury.

the electric field accelerates the positively charged ions toward the MCP for eventual detection. Before detection, however, the ion signal is amplified and converted by the MCP, into an electronic signal. These electrons, now representing the analytical signal, are accelerated in a second electric field onto a luminescent screen. The resulting luminescence is then detected by a conventional CCD camera. A schematic drawing, representing a side view of the RIID, is shown in figure 2-4.

For the applications of the RIID, λ_1 can be directed into the RIID for immediate detection, transmitted through an imaging mask into the RIID, or reflected off of an object toward the detector. In the latter two cases, λ_1 will take the shape of the imaging mask or the shape of the scattering or reflecting object.

Modes of Operation

The resonance ionization imaging detector investigated here can be operated in a variety of "modes," each providing unique information about the input signal or ionization events within the actual detector.

Detection of Charged Particles

Upon the ionization of mercury atoms in the RIID, a high voltage (V_{MCP-IW}) is applied between the MCP and front input window, or simply the atom cell. The resulting electric field accelerates the charged pair to opposite sides of the cell. The relative polarity of this applied field determines the directionality of each component. The mercury ions migrate toward the more negative region. Conversely, the photoelectrons move toward the more positive region. When the MCP is held at a more negative potential than the input window, ions are accelerated toward the MCP for ultimate detection and, hence, the RIID is said to be in *ion detection mode* or *normal mode*.

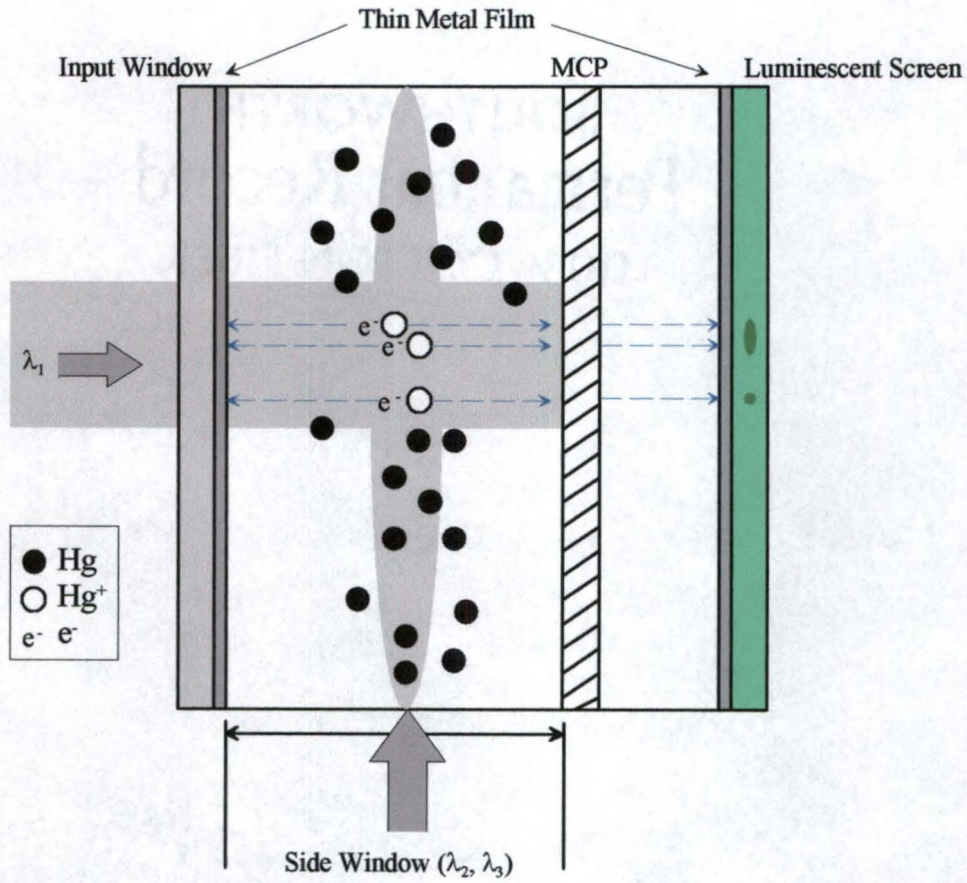


Figure 2-4. Side view illustration of the RIID for imaging mode operation. λ_2 and λ_3 are perpendicular with λ_1 and the place of the paper.

The counterpart of this technique, in which the photoelectrons are accelerated toward the MCP, is appropriately termed *electron detection mode* or *reverse mode*. Although there is no clear analytical advantage of electron detection mode, it was crucial to understanding some of the limitations of sealed-cell design RIID. This will be discussed in greater detail in the chapter 5.

Signal measurement

Perhaps of greater interest are the two forms of signal transduction in the RIID, namely *imaging* and *non-imaging modes*. Unlike the above distinction between particle detection modes, both methods of signal transduction provide useful information about signal generation. The data obtained from each detection mode are unique and can be collected simultaneously.

Imaging mode, as described above and shown in figure 2-4, relies on electronic to optical signal conversion. Electrons generated at the MCP are accelerated onto a P-20 type phosphor screen, common to conventional image intensifiers. The green luminescence from this screen can be seen visually or collected with a conventional CCD camera for further analysis. This mode allows 2 and 3-dimensional imaging information to be obtained about the incident 253.7 nm photons and their spatial distribution.

Non-imaging mode bypasses the necessity of electronic to optical signal conversion. To minimize surface charging, a thin film of metallic platinum was coated on the inner side of the phosphor screen. Instead of grounding this metal film, as originally intended, an oscilloscope was used to measure the current as electrons from the MCP pass through the film onto the phosphor screen. Therefore, the RIID is only slightly altered for non-imaging mode measurements, as shown in figure 2-5. An obvious drawback to this operational mode is the loss of 2-dimensional imaging information. This drawback is

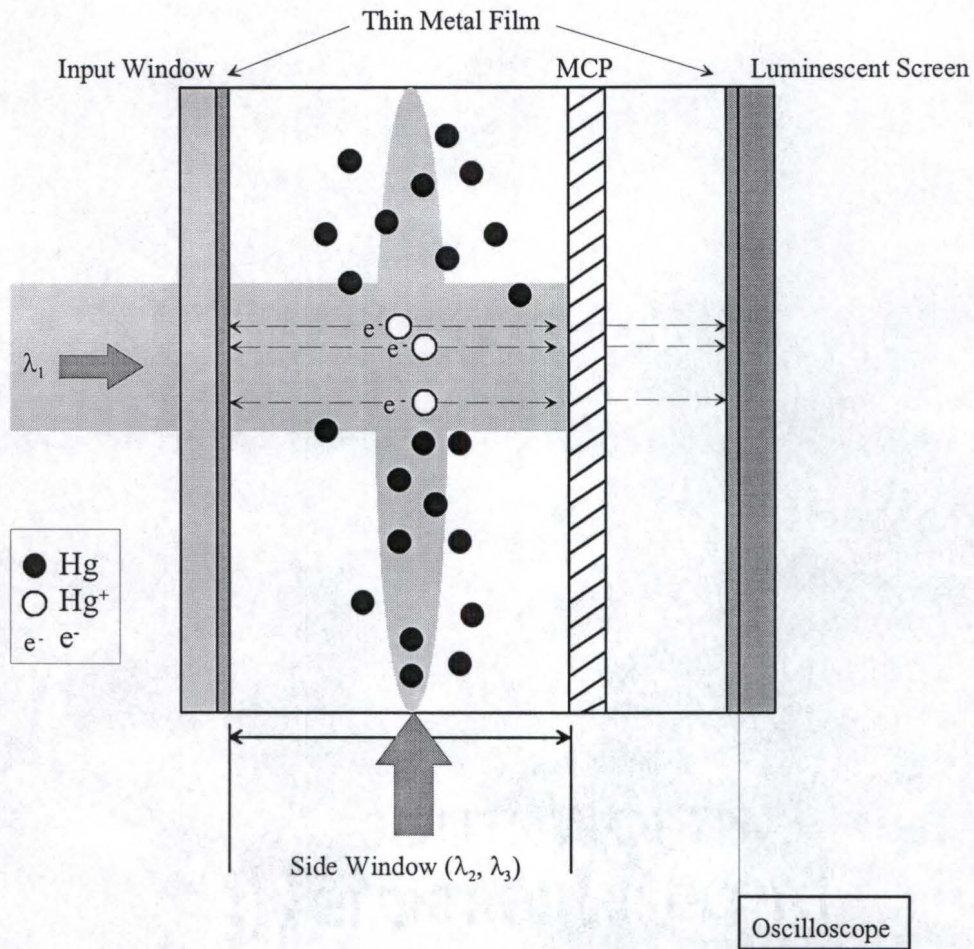


Figure 2-5. Side view illustration of the RIID for non-imaging mode operation. λ_2 and λ_3 are perpendicular with λ_1 and the plane of the paper.

easily negated as the RIID can be simultaneously operated in both imaging and non-imaging modes. The usefulness of this mode will be discussed later in chapter 4.

Experimental Description

The design of this sealed-cell mercury RIID is the product of several prototype systems to be discussed in the upcoming section. The RIID in this work was constructed, according to our design, by NPP Radian (Moscow, Russia). The compact cell is 5 cm in diameter and 4 cm in width, with a front input window diameter of 2.5 cm and side window widths of 0.7 cm. In this study, λ_2 and λ_3 are focused with a cylindrical lens into a rectangular sheet approximately 0.1 mm in width. λ_1 , which carries the imaging information in these experiments, is expanded to a 1.5 cm² spot size. Images were created by placing the imaging mask between the λ_1 beam expander and the front input window of the RIID. Amplification of the ion signal was achieved with a chevron-type microchannel plate of approximately 10^5 - 10^6 gain. The actual amplification factor of this MCP is unknown. The P-20 type ((Zn,Cd)S:Ag composition) phosphor screen used was approximately 10 μ m thick and was capable of quantum efficiencies up to 50%. To prevent surface charging of the input window and phosphor screen due to constant electron bombardment, thin metal films (5-10 nm) were coated onto the inner surfaces of each. The input window was coated with a palladium film and the phosphor screen was coated with a platinum film. The films were also used to maintain homogenous electric fields between each component and the MCP. Mercury was introduced to the cell, in excess, in the form of a titanium-mercury alloy dispenser, or *Getter* type dispenser [27]. All of the components listed here were sealed under a slight vacuum (≤ 1 atmosphere). The input window and phosphor screen are shown in figure 2-6. It should be noted that

there are several uncertainties about the construction of this RIID. These included the actual MCP amplification factor, the true thickness of the phosphor screen and metal films, the composition of the mercury dispenser, the exact pressure within the cell, and the quantum efficiency of the phosphor screen. A single high voltage power supply, coupled to a voltage divider, provided the necessary voltages to the stages of RIID detection. Figure 2-7 illustrates the high voltage divider.

The three-step photoionization schemes shown in Figure 2-3 were achieved with two dye lasers pumped by a XeCl Excimer laser with a pulse energy of 100 mJ at 308 nm and 10 Hz operation (Lambda Physik, model LPX-240i, Acton, MA). λ_1 at 253.7 nm ($6^1S_0 \rightarrow 6^3P_1$) was generated by frequency doubling Coumarin 500 laser dye (Exciton, Dayton, OH) in a Molelectron dye laser (Molelectron, Portland, OR). The remaining steps for the two color ionization scheme, $\lambda_2 = 435.8$ nm ($6^3P_1 \rightarrow 7^3S_1$) and $\lambda_3 = 435.8$ nm ($7^3S_1 \rightarrow \text{Hg}^+$), were generated by Coumarin 120 laser dye (Lambda Physik, Acton, MA). For the three color ionization scheme, $\lambda_2 = 313.2$ nm ($6^3P_1 \rightarrow 6^3D_1$) and $\lambda_3 = 626.4$ nm ($6^3D_1 \rightarrow \text{Hg}^+$), Rhodamine 101 laser dye was used (Lambda Physik, Acton, MA). When working with the two color ionization scheme, pulse energies of 10 μJ and 450 μJ were typically measured for λ_1 and λ_2 (and λ_3), respectively. Pulse energies of 10 μJ , 7.2 μJ , and 140 μJ were typically measured for λ_1 , λ_2 , and λ_3 , respectively, for the three color ionization scheme. The dye laser used for λ_2 and λ_3 generation was constructed from a Lambda Physik Scanmate dye laser (Lambda Physik, Acton, MA). The laser was constructed as a mode-free, broad band dye laser. The result was an efficient dye laser which was continuously tunable over 70 nm and had a linewidth of 14 cm^{-1} .

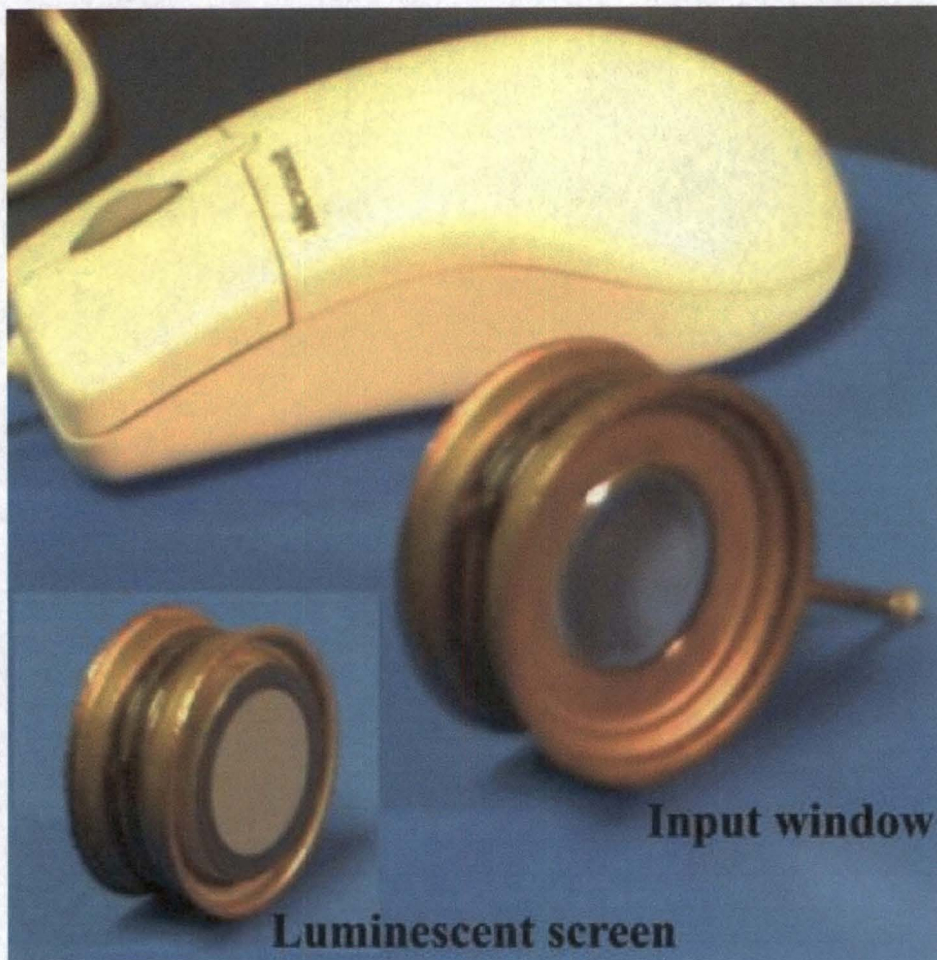


Figure 2-6. The sealed-cell mercury resonance ionization imaging detector.

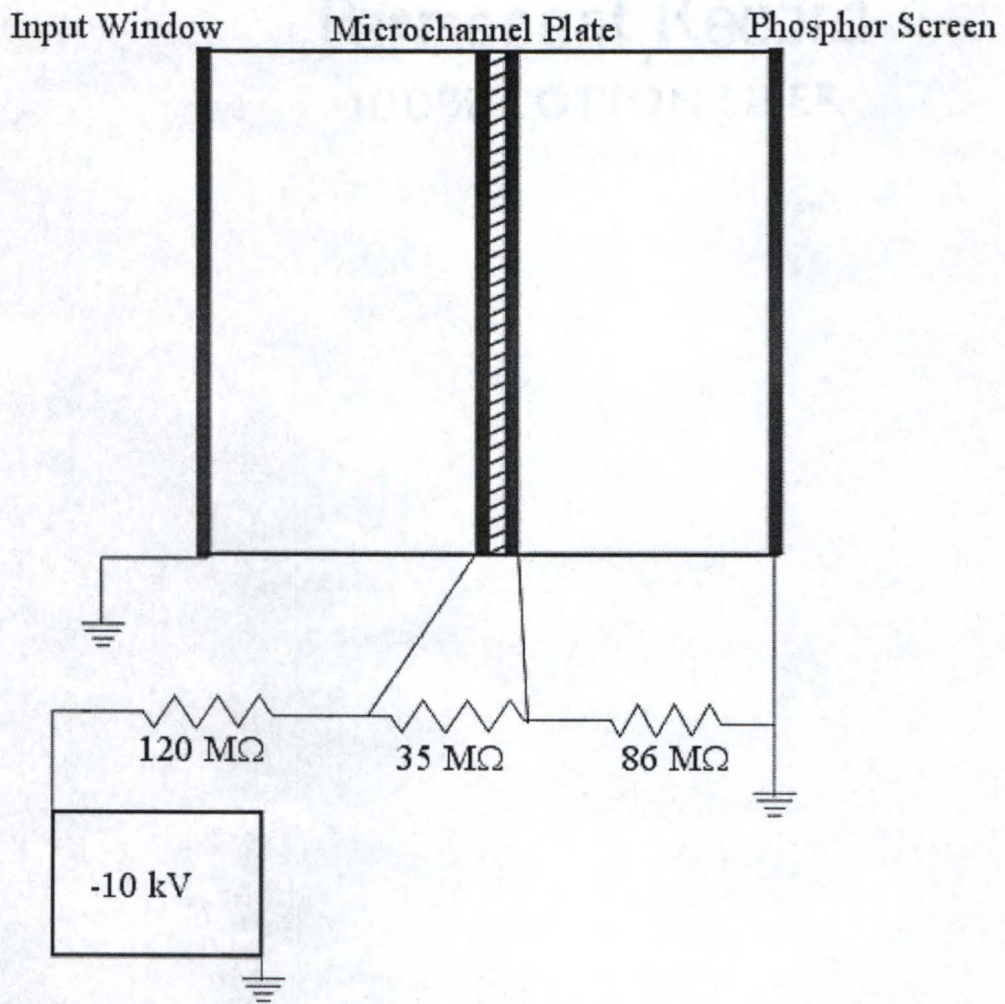


Figure 2-7. High voltage divider for the RIID.

The experimental setup described here is shown schematically in Figure 2-8. Time resolved measurements were made with a Tektronix oscilloscope (Tektronix model Tek TDS3012, Beaverton, OR).

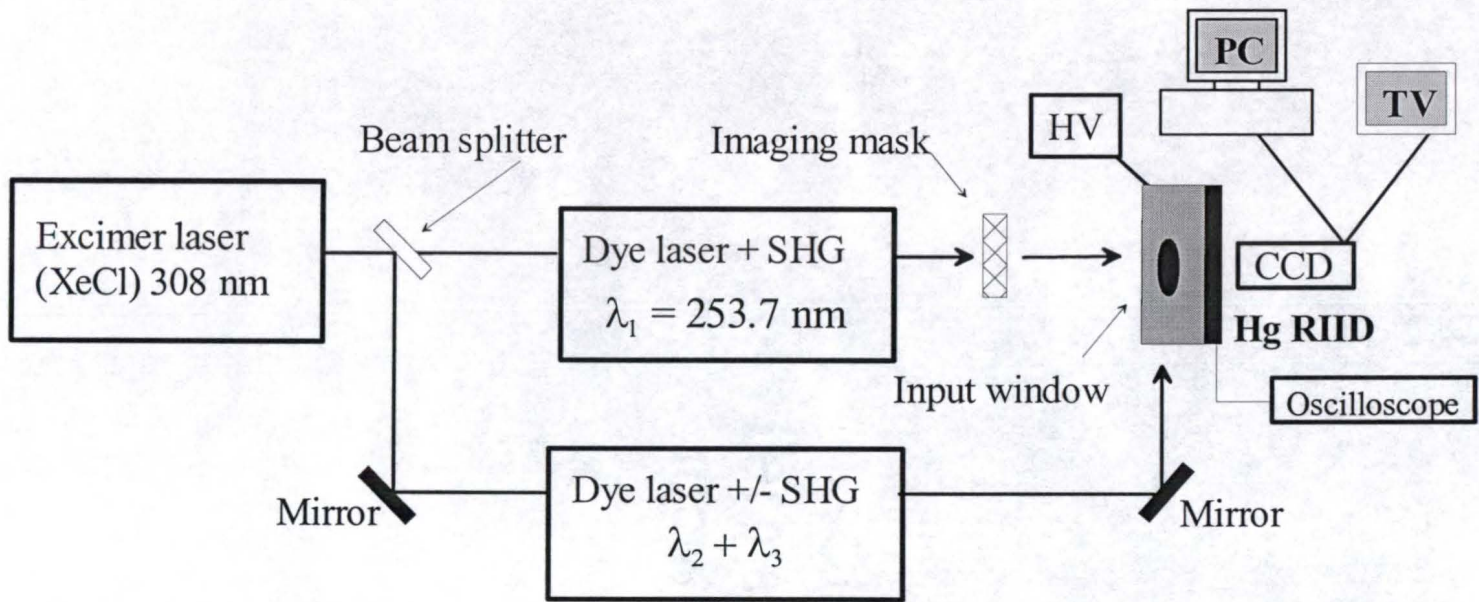
Shown in figure 2-9 are a typical series of images obtained as a function of high voltage. As shown in this series of images, there exists an operating voltage for optimal signal-to-noise and spatial resolution. The optimal voltage in figure 2-9 appears to be between 9.0 and 9.5kV. The imaging mask employed in throughout this study is shown in figure 2-10. Images were collected in real time with a CCD camera and transferred to a desktop PC via a National Instruments image acquisition board (model IMAQ, PCI-1411, Austin, TX). The monochrome CCD camera featured 510(H) x 492(W) pixels and a 0.04 Lux sensitivity (Supercircuits, model PC23C, Leander, TX).

Previous Resonance Ionization Imaging Detectors

As mentioned earlier, the RIID is still in the earliest stages of development. The first demonstration of the RIID was in 1998 [2]. The detector design in those first experiments had several drawbacks including image distortions and noise limitations due to scattered radiation within the cell. The absence of a microchannel plate also limited the sensitivity of the detector. Nevertheless, the principle of RIID operation was proven. The authors were able to demonstrate that the low pressure version of the mercury RIID was capable of acquiring images from two different wavelengths, namely 253.7 nm and 435.8 nm.

Shortly after this proof of principle, the RIID was improved by the addition of a microchannel plate and shorter cell length [4]. With these improvements, the first observation of 2-dimensional image detection with an atomic vapor imaging detector was made. The spatial resolution obtained with this detector was on the order of 0.2 mm.

Figure 2-8. Experimental setup of the RIID.



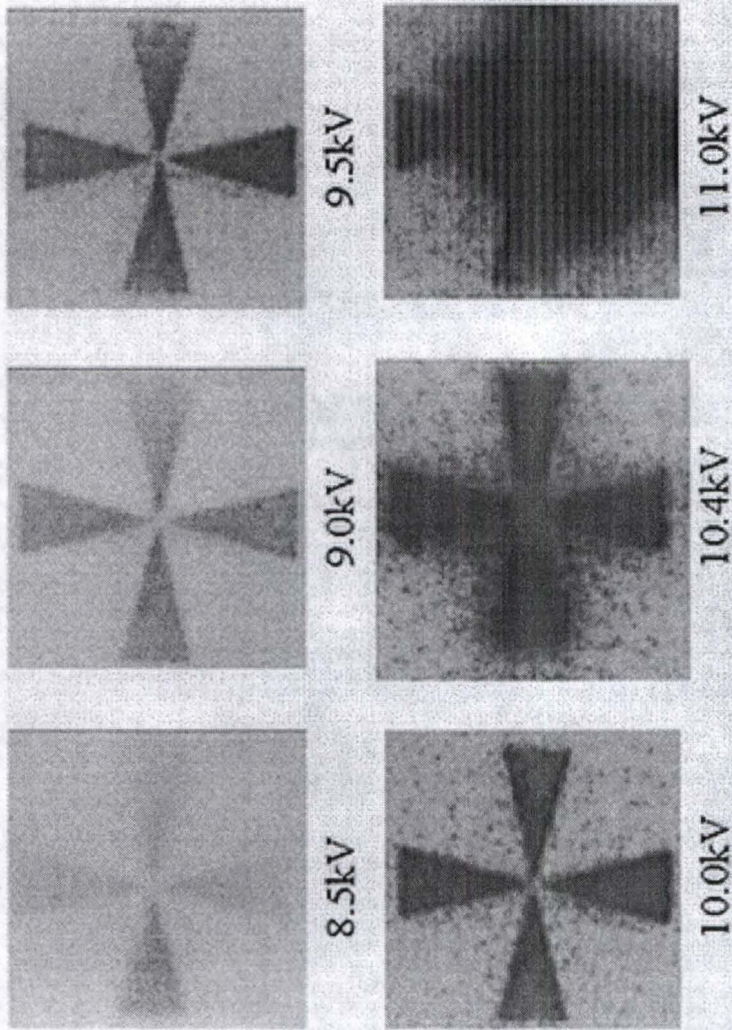


Figure 2-9. Image quality versus high voltage across the voltage divider.

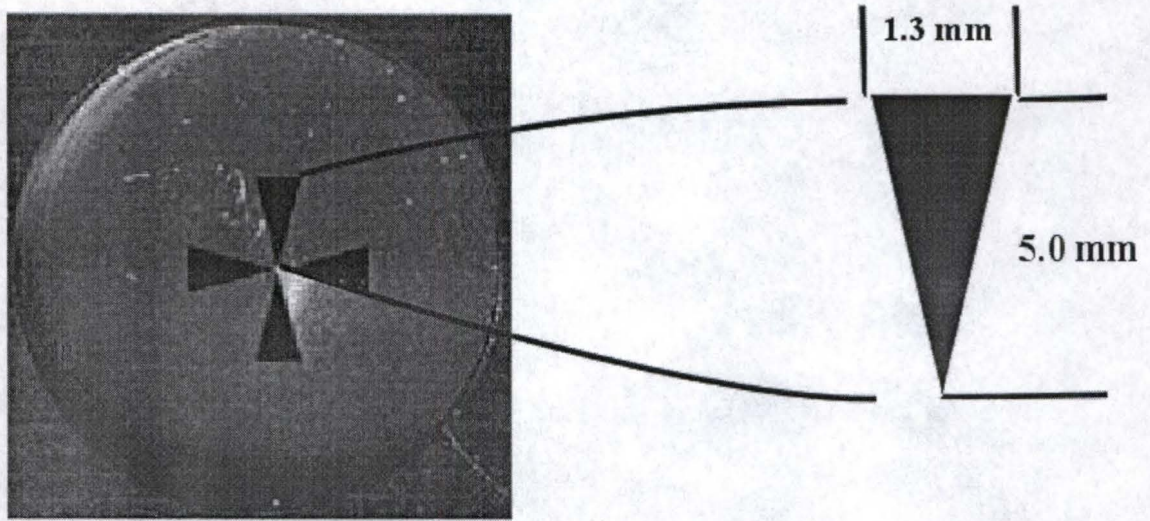


Figure 2-10. Imaging mask.

Surface charging and, thus, image distortions were the primary limitations. The detector described here is shown in figure 2-11. When comparing figures 2-6 and 2-11, the motivation behind this project becomes clear.

Following further improvement, a distortion free mercury RIID was demonstrated [28]. Spatial resolution on the order of 120 μm was achieved. These two accomplishments were the result of coating the inner surface of the input window with a thin Pt film. The 10 nm thick film reduced transmission of λ_1 by 30%, but improved imaging characteristics on several fronts. The film acted as a contact between accumulated surface charge on the input window with ground. Additionally, a more homogenous electric field was created between the input window and microchannel plate. This greatly improved the spatial resolution of the detector by forcing the ions to migrate in unaltered paths toward the MCP. The problems overcome with this version of the mercury RIID will be revisited in chapter 5.

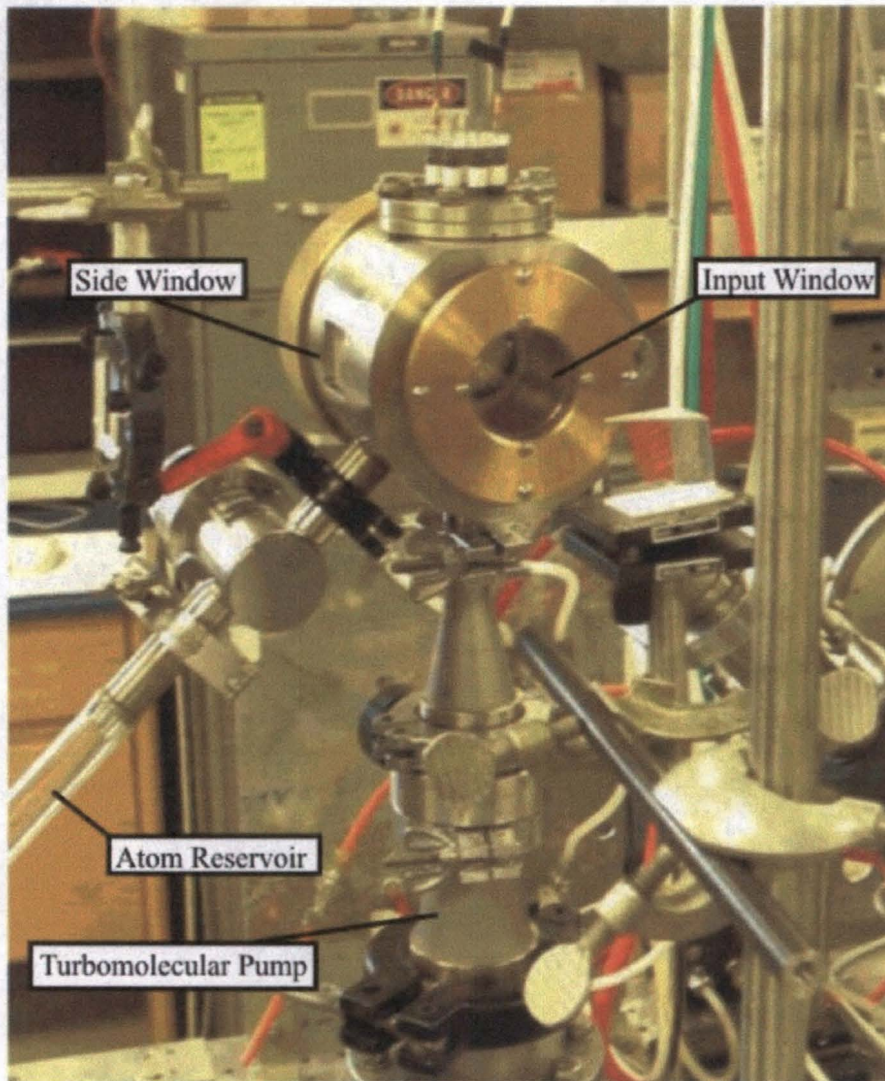


Figure 2-11. Prototype RIID with MCP.

CHAPTER 3 EVALUATION AND CHARACTERIZATION OF THE RIID

The resonance ionization imaging detector described here provides both sensitive and selective photon detection. The figures of merit for the mercury RIID make it a comparable, and in many cases superior, imaging technique for a wide range of applications. This chapter will describe the figures of merit for the RIID developed in this study and RIIDs in general. Most of the figures of merit for the RIID described here can, of course, be modeled after those of the resonance ionization detector (RID) [1,23,29].

Sources of Noise

One possible source of noise within the RIID is the non-selective photoionization of atoms and molecular dimers [1,11,29]. In the case of a mercury filled RIID, molecular dimers do not form and can be omitted from this discussion [11, 21]. As shown in figure 2-3, the final step for mercury ionization is a non-resonant transition. In this case, 435.8 nm photons are used for the photoionization from the 7^3S_1 excited state. It is possible, however, for photons with wavelengths shorter than 458 nm to also photoionize the excited state mercury atoms. As a result, non-selective ionization could occur and its associated signal would be detected. Although this source of noise was not observed for the RIID presented here, its potential certainly exists. Various optical filters were used to show that the ionization only occurred as a result of $\lambda_3 = 435.8$ nm.

Another source of noise in the RIID is the generation of electrons, via the photoelectric effect. In this case, λ_1 strikes a metal surface of a given work function and

an electron is ejected. These electrons may be ejected from the MCP or from the metal film coating on the input window [2]. When the detector is operated in ion detection mode, only the electrons generated at the MCP are problematic. This effect will be discussed in detail in the following chapter.

A final source of noise in imaging mode RIID operation is background luminescence. This background luminescence is more pronounced at high voltages and is observed as random "spots" on the phosphor screen. Because this luminescence is observed even without incident laser radiation, this noise likely arises within the final stage of detection [31]. A probable explanation of this noise is autoelectronic emission from the MCP [31-33]. By operating at lower voltage, when λ_1 is sufficiently high, this source of noise can be eliminated [34].

Spectral Bandwidth and Range

The most significant advantage of the RIID, when compared to conventional imaging detectors, is the selectivity with which photons are detected. In the case of the RIID, the figure of merit which best represents selectivity is the spectral bandwidth (s) [35]. The spectral bandwidth of the RIID is limited by the absorption linewidth of the contained atomic vapor. For that reason, it is useful to consider the spectral bandwidth as a measure of the background rejection of the detector. Photons which are not within this spectral bandwidth are rejected by the detector.

For the mercury RIID described here, the Doppler broadened linewidth of the mercury vapor is about 25 GHz. This linewidth is achieved by summing the linewidths of mercury's 7 stable isotopes. It has been calculated that the background rejection for such an atomic vapor, at a frequency shift of 0.6 cm^{-1} , should be on the order of $10^{-3} \%$ [1,29].

The observed frequency response, corresponding to the spectral bandwidth, is shown in figure 3-1 when the RIID is operated in the non-imaging mode. The level of background rejection, when λ_1 is detuned by 0.6 cm^{-1} , is about 45 %. This level improves to over 97 % at a 4.0 cm^{-1} frequency shift. When operated in imaging mode, these figures of merit are not as impressive. At a frequency shift of 0.6 cm^{-1} , the rejection level is 30 % and only about 65 % at 4.0 cm^{-1} . This is most likely due to photoelectric signal generation, which is not influenced by small frequency shifts as shown here. The photoelectric and resonance ionization signal cannot be discerned in the imaging mode. A discussion of photoelectric signal generation will be presented in the following chapter.

The observed 25 GHz linewidth for the isotopic mixture, used in this work, is the result of Doppler broadening and hyperfine level splitting. Figure 3-2 illustrates the isotopic and hyperfine splitting components of the $6^1\text{S}_0 \rightarrow 6^3\text{P}_1$ transition at 253.7 nm [36]. The natural atomic linewidth of the mercury isotopes shown in figure 3-2 is on the order of 1.4 MHz. However, Doppler broadening can increase each to about 1 GHz. Doppler broadening of atomic lines results from the statistical distribution of velocities of the absorbing atoms [35]. The Doppler effect causes a distribution in the measured frequencies that is directly related to this velocity distribution. When Doppler-free techniques are employed with a monoisotopic vapor cell, the spectral bandwidth can approach the natural atomic linewidth of a single mercury isotope of 1.4 MHz. Doppler-free techniques refer to experiments in which the velocity, and thus frequency, distribution is minimized in some fashion [37]. Such techniques include *saturation*

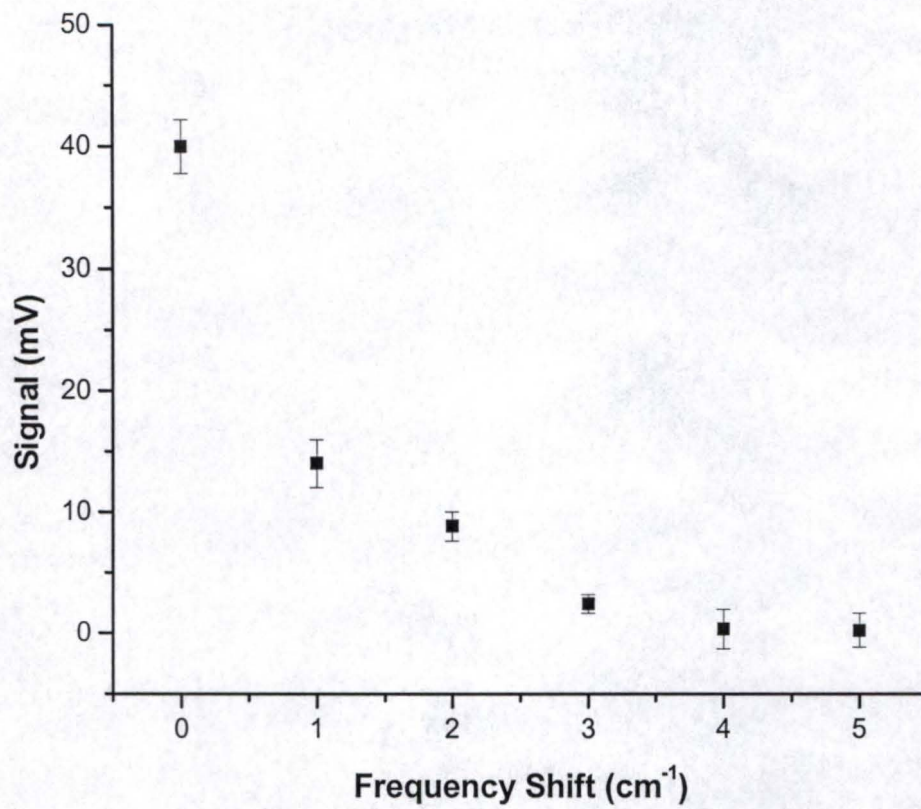


Figure 3-1. Spectral response of the RIID in non-imaging mode as λ_1 is detuned away from the center of resonance line.

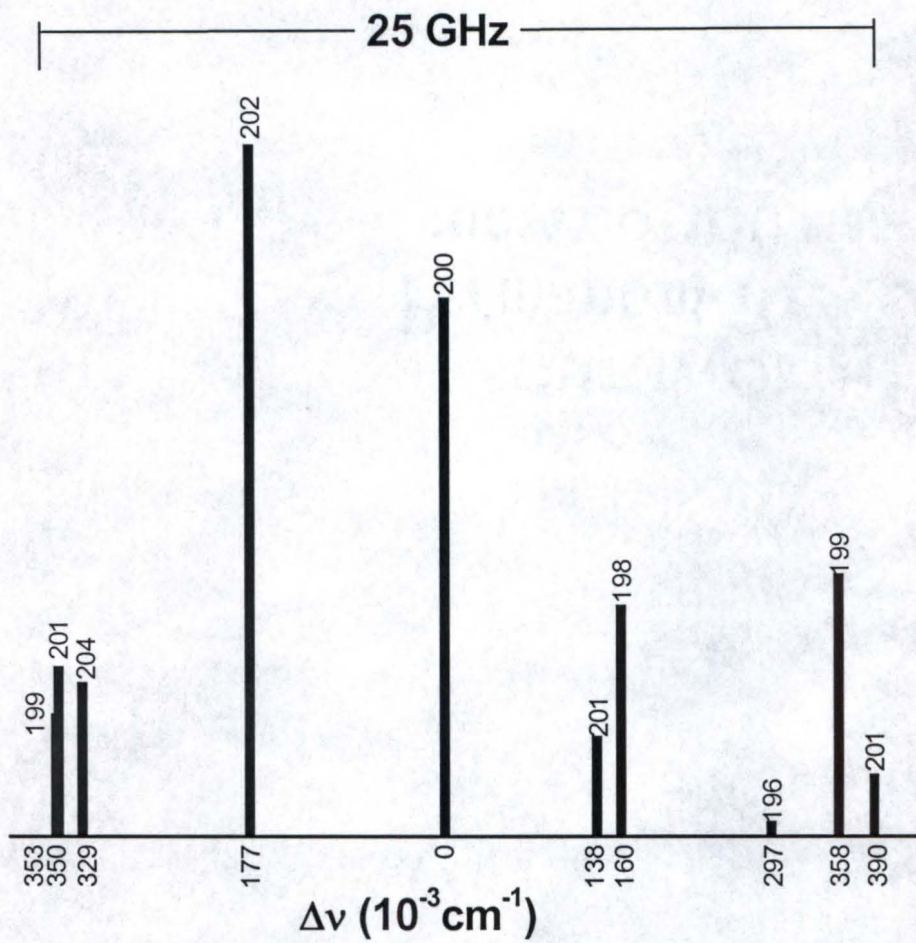


Figure 3-2. Isotope and hyperfine splitting of mercury's ground state transition ($6^1S_0 \rightarrow 6^3P_1$) (adapted from Grossman *et al.*) [36].

spectroscopy, lambda dip spectroscopy, and collimated molecular beam spectroscopy [35,38]. However, the RIID design discussed here does not permit Doppler-free techniques to be applied. Future RIID designs could be designed to allow such Doppler-free measurements.

When Doppler-free measurements are not accessible, differential imaging techniques can also be used to improve upon the spectral bandwidth. Differential imaging, as applied to the RIID, refers to a technique in which image intensities are measured as a function of λ_1 frequency. Image intensity will increase as λ_1 approaches the center of the resonance transition. For example, it has been shown that 80 MHz frequency resolution is achievable with UBID differential imaging techniques [39]. In that study, a fluorescence scheme of photon detection was used rather than ionization.

The spectral working range of a particular RIID is inherently small, being limited to the linewidth of the first atomic transition. For the mercury RIID, the maximum working range is 25 GHz at 253.7 nm, which corresponds to 253.7 ± 0.0002 nm. This narrow band is responsible for the selectivity of the RIID, but limits the working range for many applications. By using a different atomic vapor, each with unique λ_1 and s , the working range of the RIID could be shifted and, perhaps, slightly improved. When both laser availability and engineering limitations are considered, there are 10 elements suitable for use as the RIID's active medium [1,11,12]. These elements are listed in table 3-1.

Element	Ionization Energy (eV)	λ_1 (nm)	Reference
Li	5.35	670.8	[40,41]
Na	5.14	589.0, 589.6	[42-44]
K	4.34	404.7, 766.5	[45,46]
Ca	6.11	422.7, 616.2	[47,48]
Rb	4.18	420.2, 780.0, 794.8	[49-51]
Sr	5.69	460.7, 689.3	[48]
Cs	3.89	459.3, 852.1, 894.3	[52]
Ba	5.21	553.5, 791.1	[53-55]
Hg	10.44	253.7, 312.8	[56,57]
Tl	6.11	276.8, 377.6	[48]

Table 3-1. List of elements suitable for use as the RIID's active medium.

Sensitivity

The high sensitivity of most RID and RIID systems arises from the final, non-resonant ionization step. The efficiency for this photoionization step can approach 100 % [11,22,58]. By saturating the 6^3P_1 excited state (see figure 2-3), each 253.7 nm photon absorbed should then be detected. Using a three-step resonance excitation scheme, followed by collisional ionization in a buffer gas, Matveev *et al.* achieved single photon detection in a RID [23]. It is therefore possible that single photon detection limits might be achieved with the RIID.

Although the Hg RIID presented here did not achieve this lower detection limit, relatively low light conditions were detected. When operated in the imaging mode, fewer than 1,000 incident photons were detected via image summation [31]. When λ_1 intensity is low, it was necessary to sum several images (10 – 20) to improve the S/B. In the case of 16 image summations, the S/B is improved 15 times.

When operated in non-imaging mode, a lower photon detection limit can be achieved. A 5.0 mV signal can be discerned from the noise, which corresponded to a S/N of 3. This, in turn, correlated to about 540 incident photons. In this case, the λ_1 beam was focused into a small absorbing volume for more efficient ionization. When λ_1 was expanded for 2-D experiments, the limit of detection of incident photons was degraded to about 900. These types of experiments will be covered more thoroughly in the following chapter.

Spatial Resolution

The spatial resolution obtainable with conventional CCD cameras and image intensifiers is on the order of about 30 μm [33,59]. It has been calculated that the RIID

could achieve comparable results [1,10]. This is realized as the second stage of RIID detection (MCP to phosphor screen) is identical to that of conventional image intensifiers [60]. For various reasons, ranging from cell engineering to imaging distortions, this degree of spatial resolution has not been achieved. However, for the RIID described in this work, a spatial resolution of 80 μm has been observed. Shown in figure 3-3 is an image obtained with this detector, corresponding to a spatial resolution of 80 μm .

Several improvements to cell design could be made to improve upon the obtainable spatial resolution. Such include a shorter flight path for ions to the MCP and a shorter distance between the MCP and phosphor screen. In principle, the phosphor could be coated directly onto the MCP. However, as will be shown in upcoming chapters, there are disadvantages of employing these types of improvements.

Temporal Resolution and Response

In principle, the time resolution of the RIID ($\Delta\tau_{RIID}$) is limited by two factors: the flight time of the ion from generation to the MCP (τ_F) and the rate of ionization (s^{-1}) due to the additional laser radiation (R_{ADD}).¹ Equation 3-1 relates these terms mathematically.

$$\Delta\tau_{RIID} = \sqrt{\tau_F^2 + \left(\frac{1}{R_{ADD}}\right)^2} \quad (3-1)$$

When ionization occurs close to the MCP, a voltage can be applied such that τ_F can be as low as 200 ps. From this, it is apparent that the ultimate limit upon temporal resolution in the RIID will be the rate of ionization. The rate of ionization by the second and third step

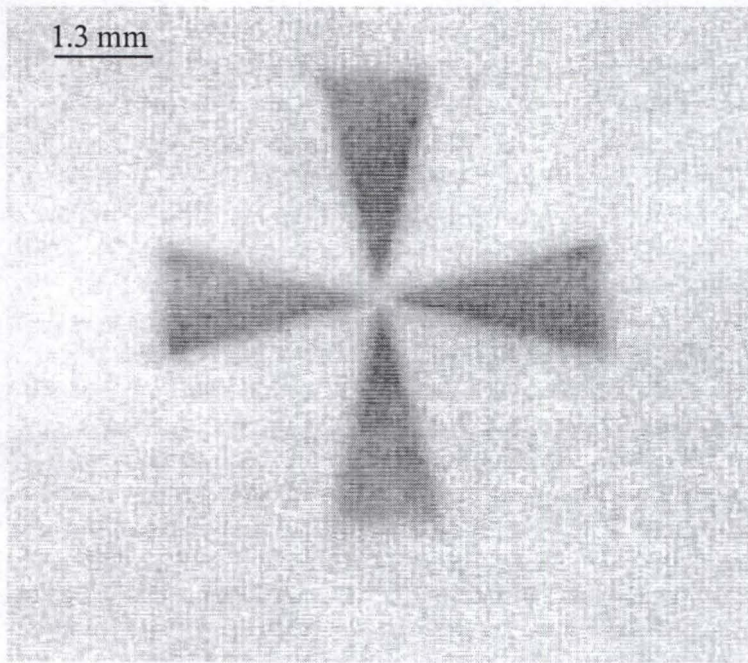


Figure 3-3. RIID captured image with 80 μm spatial resolution.

photons is limited by the lifetime of their respected excited state. For the ionization scheme shown in figure 2-3, the 7^3S_1 state has a lifetime of 8 ns [61]. For this reason, the Hg RIID described here could achieve a temporal resolution of 8 ns. However, as in the case of spatial resolution, experimental limitations prevent this observation. The temporal resolution for the detector described in this study was limited to the frequency at which the ionizing lasers were operated (1 – 10 Hz).

Quantum Efficiency

The following discussion of quantum efficiency will pertain to RIIDs in general, rather than the detector described in this dissertation. Experimental limitations stemming from the design of the sealed cell detector prevented a direct measurement of this figure of merit.

Quantum efficiency (q) for the mercury RIID is defined as the ratio between the number of ions created to the number of input λ_1 photons. A more practical definition is shown in equation (3-2).

$$q = \alpha\eta \quad (3-2)$$

The quantum efficiency is the product of α , the absorption factor of the atomic vapor, and η , the ionization efficiency; η is defined as the ratio of the number of ions created to the number of 7^3S_1 excited state mercury atoms. Values of 0.1 have previously been obtained for a mercury filled RID [23]. In this study, the authors used relatively weak lasers for this measurement. When higher energy lasers are employed (> 1 mJ/pulse),

there are no fundamental limitations preventing an ionization efficiency near 100 % [1,12,36].

The maximum value of α will, of course, occur at the center of the absorption line. The absorption factor α is defined by the following equation.

$$\alpha = 1 - e^{-n\sigma l} \quad (3-3)$$

In equation 3-3, n is the density (cm^{-3}) of the atomic vapor at a given temperature, σ is the cross section (cm^2) for the ground state transition, and l is the optical path length (cm). In the case of the Hg RIID at room temperature, $n = 4 \times 10^{13} \text{ atoms}\cdot\text{cm}^{-3}$ and $\sigma = 6 \times 10^{-13} \text{ cm}^2$.

Under these conditions, it has been calculated that a quantum efficiency greater than 90 % can be achieved for a mercury filled RIID [1]. It has also been shown that a quantum efficiency greater than 60 % can be achieved for at least 23 elements below 300 °C [12] (see table 2-1). As discussed above, atomic vapors other than mercury would broaden the working range of the detector. The possibility for near unity quantum efficiency further illustrates the capabilities of the RIID as a sensitive photon detector.

CHAPTER 4 TIME RESOLVED MEASUREMENTS IN THE RIID

Non-imaging mode operation of the RIID involves a current measurement rather than an image capture. Upon the resonant photoionization of the contained mercury vapor, the signal ions are accelerated toward the MCP for amplification and eventual detection. This electronic signal is converted into an optical signal, via the phosphor screen, or detected directly. The electronic signal is measured as electrons from the MCP pass through a thin metal film in route to the phosphor screen. This platinum thin film, normally grounded to relieve surface charging, in this case, is connected to an oscilloscope. Because these electrons still reach the phosphor screen, both non-imaging and imaging modes can be simultaneously performed.

Photoelectric effect in the RIID

A key advantage of the RIID is its ability to selectively detect minimal photons in the presence of high background. However, a source of noise in the RIID is the signal generation due to the photoelectric effect (PE) by high levels of λ_1 signal photons. In experiments with an intense λ_1 source, not all 253.7 nm photons are absorbed by the Hg vapor. In this case, λ_1 is transmitted onto the surface of the MCP and the photoelectric effect is observed. The MCP response to these PE electrons is identical to that of the mercury ions. An image can be created on the phosphor screen, which corresponds to this second source of signal (from transmitted λ_1). This is shown experimentally when λ_2 and λ_3 are blocked from the RIID. Without these final transitions, mercury ionization

will not occur. The resulting image is created entirely by electrons generated from the photoelectric effect on the surface of the MCP. Under normal operating conditions, when the three beams ($\lambda_1, \lambda_2, \lambda_3$) needed for ionization are present, the image formed contains both PE and ionization components. These two components of the signal cannot be discerned in the imaging mode.

Temporal Response of the RIID in Non-imaging Mode

The non-imaging mode is useful to resolve the PE and resonance ionization components of the signal. Shown in figure 4-1 is a time resolved measurement, typical of non-imaging mode RIID detection. The location within cell, where each signal component is generated, is given by the measured time. This measurement can be thought of as a "flight" time for the ion to reach the MCP. Since the PE signal is generated on the surface of the MCP, $t = 0$ is assigned to the PE peak. Ionization of the mercury vapor takes place at some depth within cell, so the ionization component will have a longer travel time. For the example shown in figure 4-1, Hg ionization occurred in the center of the RIID. From that point, it took the mercury ion 350 ns to reach the MCP. The peak detected at approximately 100 ns will be discussed later in this chapter.

Effect of λ_2 and λ_3 Position within the RIID

Figure 4-2 illustrates how the location of the ionization region can be varied with the position of λ_2 and λ_3 . The flight time of the Hg ion can, of course, change as the sheet of λ_2 and λ_3 is shifted between the input window and MCP. Shown in figure 4-3 is the non-imaging RIID signal when the ionization region is shifted away from the input window toward the MCP. A difference of nearly 75 ns in flight times is observed for the resonance ionization signals in this case.

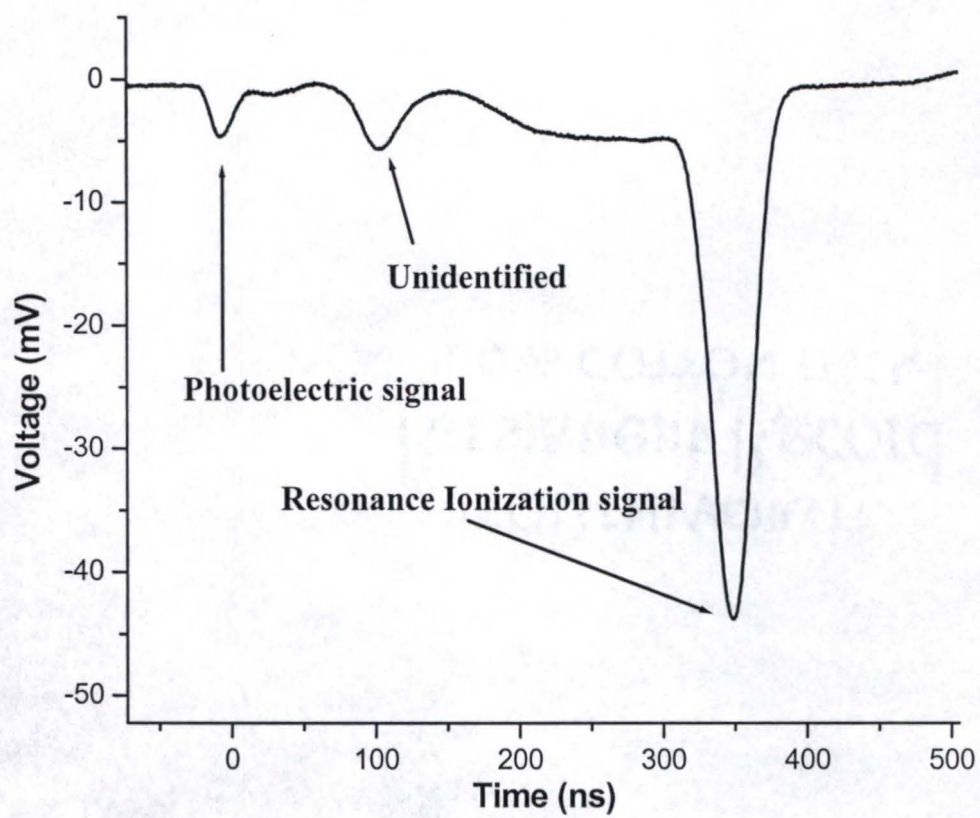


Figure 4-1. Time resolved measurement in the RIID.

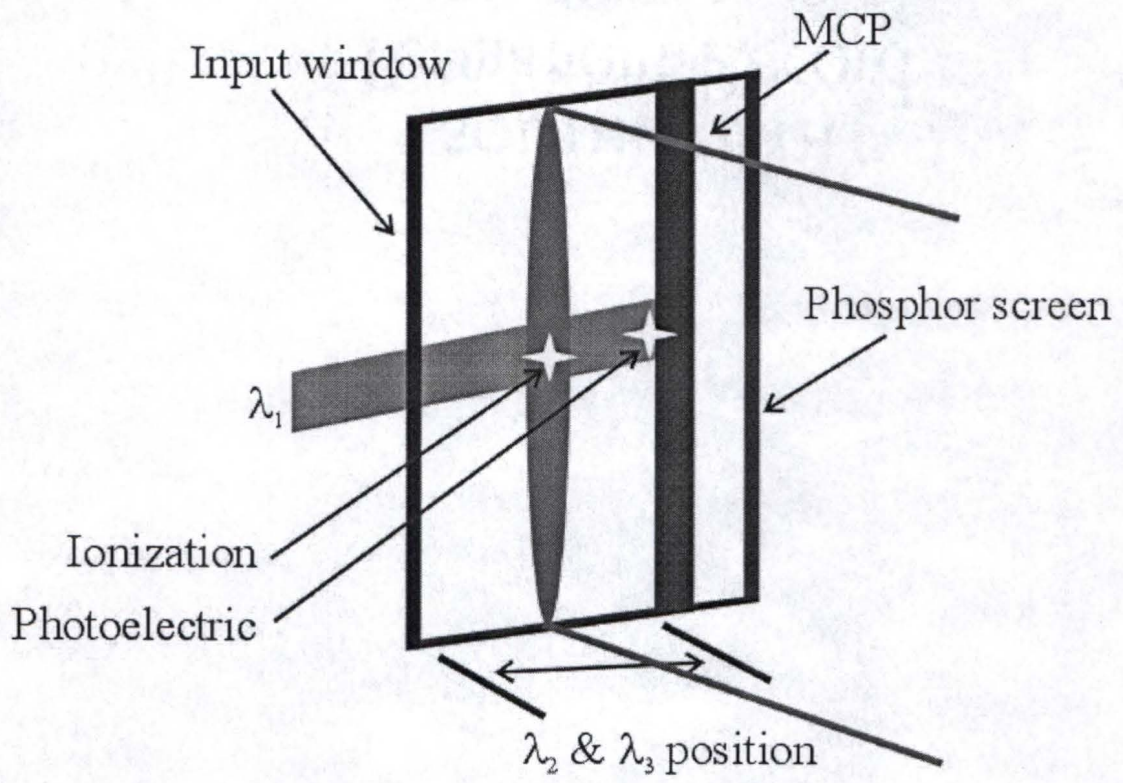


Figure 4-2. RIID schematic showing λ_2 and λ_3 position and signal generation.

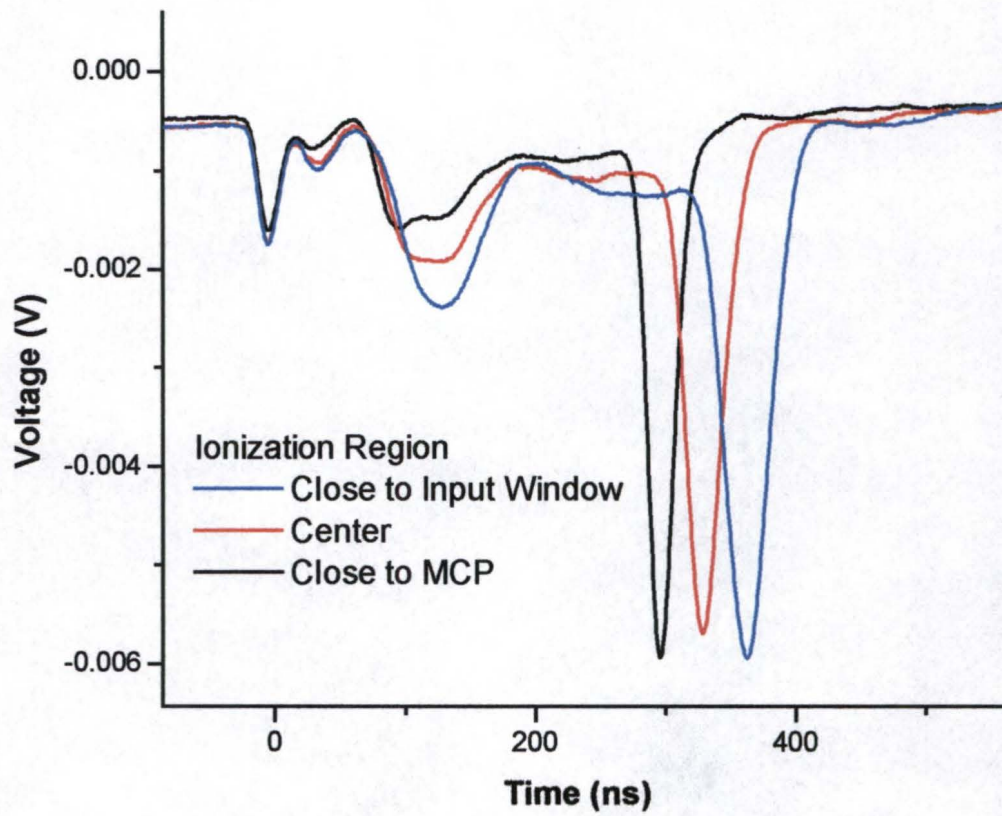


Figure 4-3. Non-imaging mode signal when the ionization region shifted away from input window toward the MCP.

There are several reasons for varying the position of the ionization region in this fashion. One such reason, as discussed above, is to allow the separation of PE and ionization signal. This is achieved by having the ionization region close to the input window, such that the flight time of the mercury ion is relatively long. Another reason to have the ionization region close to the input window is improved ionization efficiency, and thus a lower photon limit of detection. This arises from the fact that most λ_1 photons are absorbed within the first few millimeters of the absorption cell. λ_2 and λ_3 should also be directed into this region of the cell for most efficient ionization.

The primary advantages of having the ionization region closer to the MCP are observed in the imaging mode of detection. The spatial resolution of the RIID can be improved when ionization events occur close to the MCP. Although steps have been taken for a homogenous electric field between the input window and MCP, even slight differences in this accelerating field will result in image distortions. Decreasing the flight path of the ion will decrease the probability of ion diffusion within the cell and, hence, improve spatial resolution. Figure 4-4 shows images in when the ionization region is moved between the input window and MCP. A similar problem to this one, namely image distortions, will be also be minimized when ionization occurs close to the MCP. These phenomena will be discussed in detail in the following chapter.

Effect of High Voltage Application

During the first stage of detection in the RIID, a high voltage ($V_{\text{MCP-IW}}$) is applied between the input window and microchannel plate. The electric field created between these two components acts as an acceleration field for the formed ions.

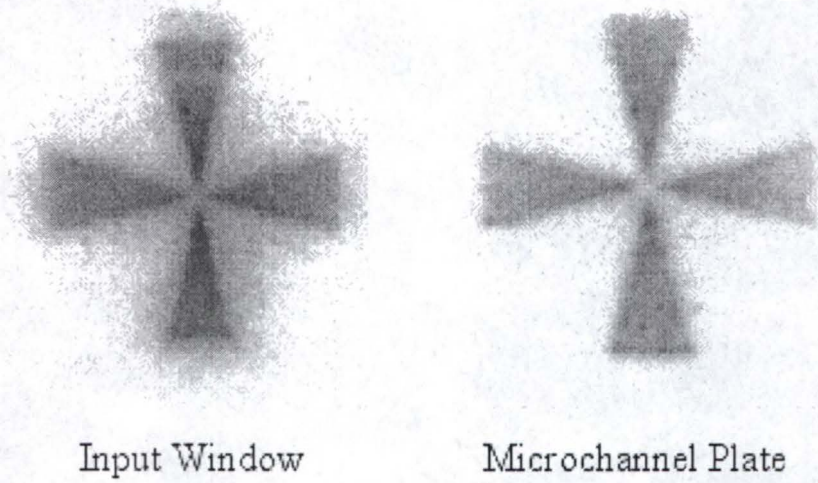


Figure 4-4. Imaging mode detection for λ_2 and λ_3 close to input window and MCP.

The flight time, in seconds, of the ion is inversely proportional to the electric field strength [9].

$$\tau_F = \sqrt{\left(\frac{m}{z}\right) \frac{L^2}{2V}} \quad (4-1)$$

This relationship is shown in equation 4-1, where $\frac{m}{z}$ is the mass to charge ratio (kg) of the mercury ion, L is the length of the flight tube (or width of the RIID) (m), and V is the applied voltage (volts). It is predicted from this equation that the flight time of the mercury ions will be reduced as V_{MCP-IW} is increased. This is shown experimentally in figure 4-5. The ionization region is held constant in the center of the cell in this example, while V_{MCP-IW} is varied. Similar to the example shown in figure 4-3, the flight times of the ion signals are altered. As the V_{MCP-IW} is increased between 0.95 and 1.40 kV, the flight times are varied between 624 and 682 ns. These are much longer flight times as compared to the example in figure 4-3, in which $V_{MCP-IW} = 4.5$ kV. The magnitudes of both the PE and ion peaks are also altered. This is expected when the voltage scheme shown in figure 2-6 is used, as the gain of the MCP is increased as V_{MCP-IW} is increased. When the RIID is operated in the imaging mode, this may result in a limiting source of noise.

Signal-to-Noise Ratio in Non-imaging Mode

An advantage of non-imaging mode detection is an improved S/N. This is achieved by the temporal resolution of the ionization signal from the PE background. Upon resolution of these signal components, the limiting noise is reduced by several orders of magnitude. A discussion of limiting noise sources was described in the previous chapter.

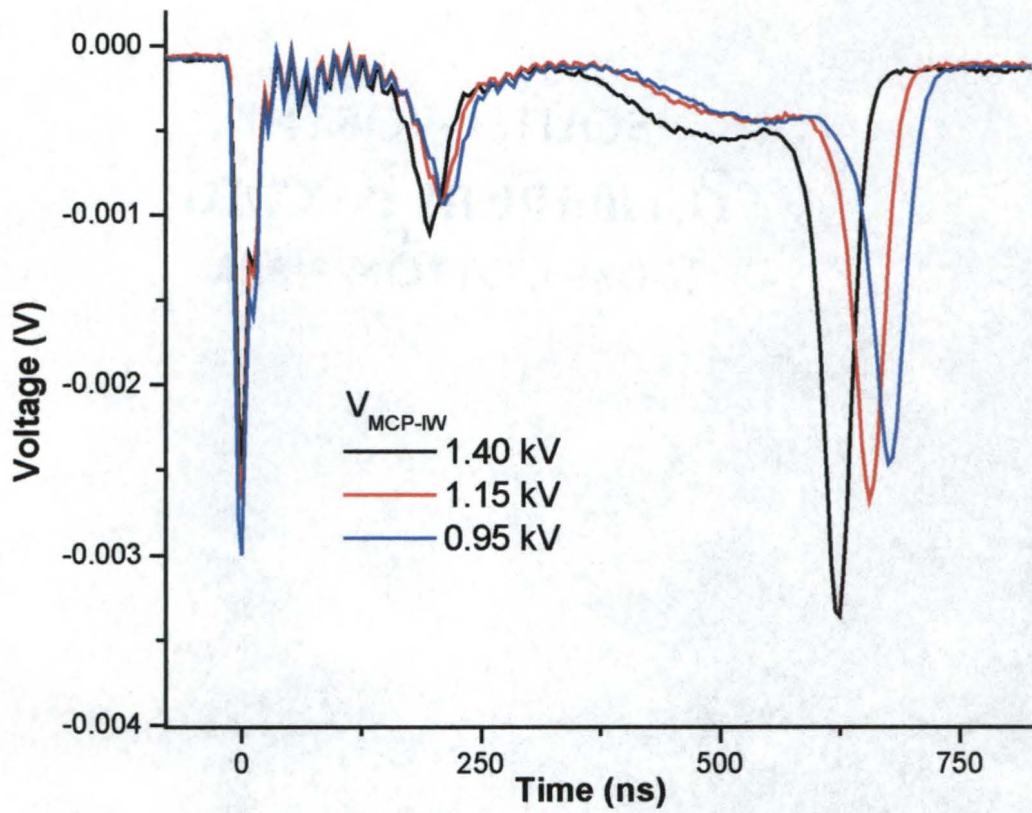


Figure 4-5. Effect of high voltage upon non-imaging mode signal.

A given number of incident photons can be achieved by attenuating λ_1 with neutral density filter combinations. Figure 4-6 shows the detection of approximately 10^9 incident 253.7 nm photons. In this case, a S/N of 135 is observed. Shown in this figure is non-imaging signal as well as the electronic noise measurement when λ_1 is not present. Noise is calculated as the standard deviation of the latter case. When the number of incident λ_1 photons is decreased to 10^5 , the applied voltage must be increased from 9.0 kV to 9.5 kV. As shown in figure 4-7, the S/N is degraded from 135 to 64. It is implied from these data that the applied high voltage ultimately limits the S/N and, thus, the limit of photon detection in the non-imaging mode.

Unidentified Ionization Component

As shown in the previous figures of this chapter, an additional signal component exists between the PE and ionization peaks. Time was devoted in this work to the identification of this peak. However, experimental limitations and uncertainties concerning the cell's construction have not allowed a positive identification. Furthermore, this unidentified component is only discernable in the non-imaging mode. Possibilities of the origin of this peak are deduced from non-imaging mode data shown here.

The hypothesis for these experiments arises from flight time calculations with equation 4-1. In this hypothesis, it is assumed that the signal of interest originates within the atom cell of the RIID. Secondly, the unknown ion causing this signal must have a lower m/z than does the mercury ion. Possibilities for a lower m/z include singly charged ions, such as sodium and potassium ions, or doubly charged mercury ions.

The possibility of doubly charged mercury ions is not likely, based only on a few experiments. As shown above, the flight times for ions to reach the MCP can be varied

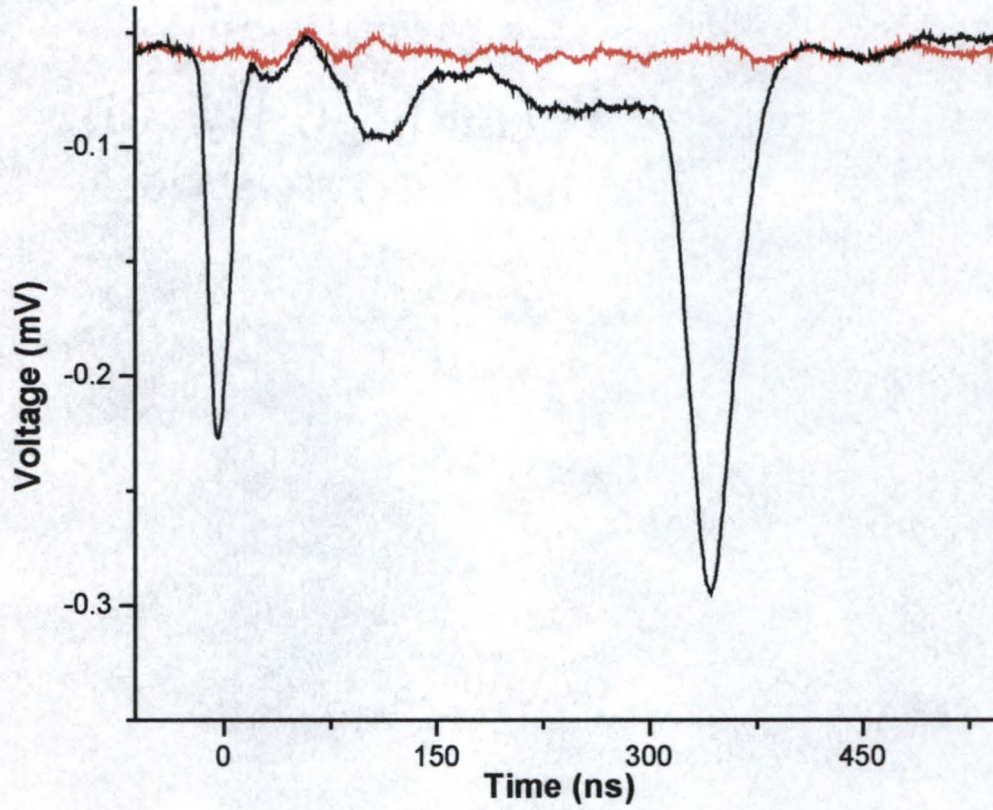


Figure 4-6. Non-imaging mode signal-to-noise ratio of 135 for $V = 9.0\text{kV}$ and 10^9 incident photons. (—) shows noise due to λ_2 and λ_3 beams only; (—) shows signal when all three beams are present.

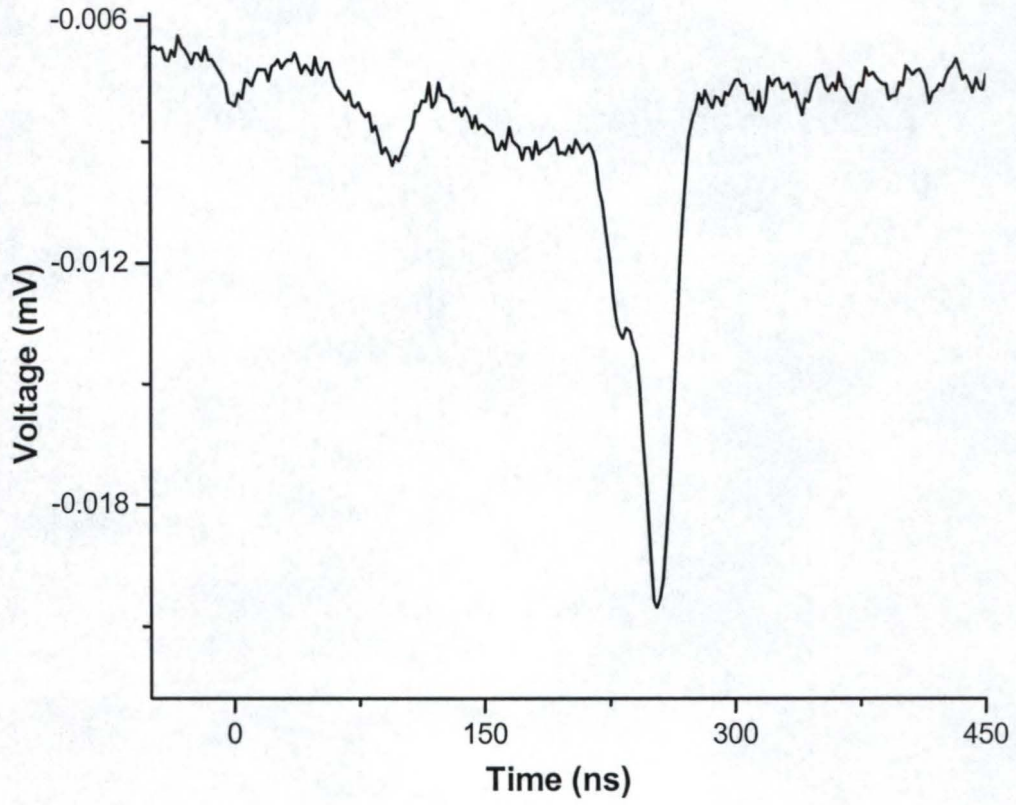


Figure 4-7. Non-imaging mode signal-to-noise ratio of 64 for $V = 9.5\text{kV}$ and 10^5 incident photons.

with high voltage. Figure 4-5 illustrates the effect of high voltage upon flight times. From equation 4-1 it is predicted that Hg^+ and Hg^{+2} will have different flight times, but should change proportionally with each other as the applied voltage is varied. In other words, the separation between these two peaks should remain constant as the high voltage is increased. The relative intensity of each peak should also change proportionally as MCP gain is increase. However, this behavior is not experimentally observed. Figure 4-8 shows the separation of these two peaks as a function of $V_{\text{MCP-IW}}$. From this plot, we see that the flight time of the resonance ionization signal is influenced more by voltage than is the unknown component. In figure 4-9, the intensity ratios of these peaks is shown as a function of voltage. Similar to the previous example, the intensity of the resonance ionization signal is affected more by voltages changes than is the unknown component. These two experiments show that unknown signal component is not likely due to doubly charged mercury ions.

Several important implications can be extracted from these data. The unknown signal component originates from a positively charged ion. Proof of this is provided by the experimental observation of detecting this component only in the ion detection mode. Any negatively charged species would be accelerated toward the input window. Furthermore, as proof against a doubly charged mercury ion suggests, this positive ion must have a lower m/z than mercury. Calculations show that the molecular weight of these ions were in the range of 20 - 55 amu assuming singly charged ions. This wide range of molecular weights does not allow further deductions. One final consideration is the response of the unknown signal component to λ_1 , λ_2 and λ_3 photons. It was observed that this peak was dependent upon both λ_1 and λ_2 (and λ_3). In the absence of λ_1 , as

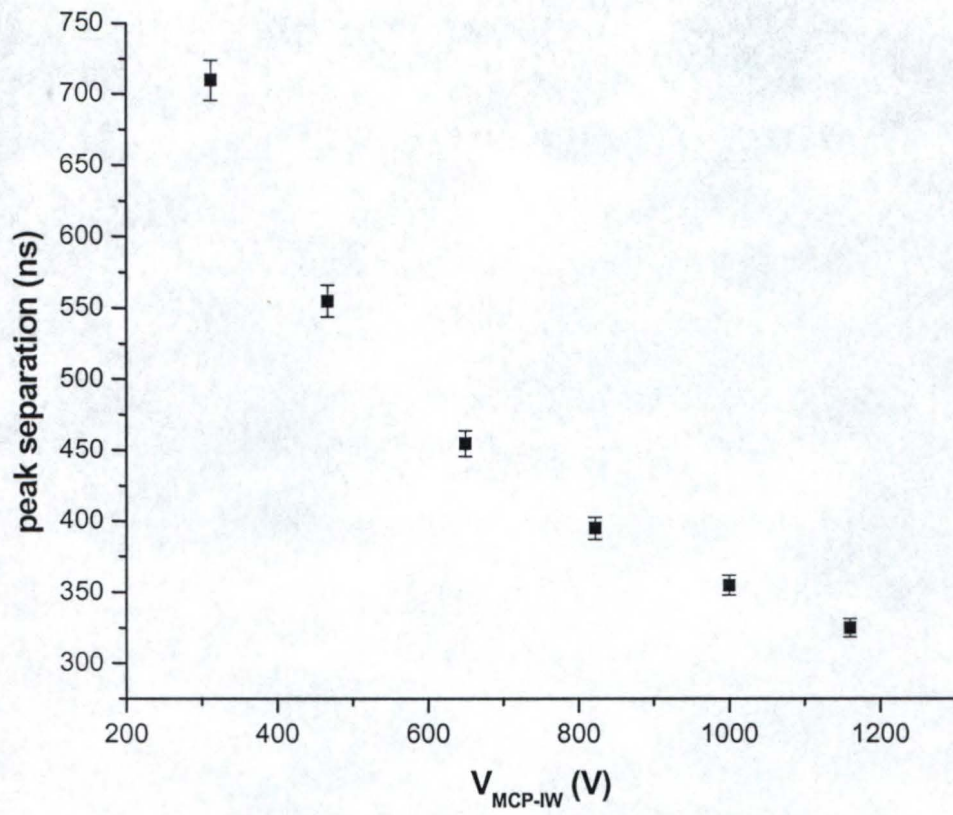


Figure 4-8. Peak separation as a function of V_{MCP-IW} .

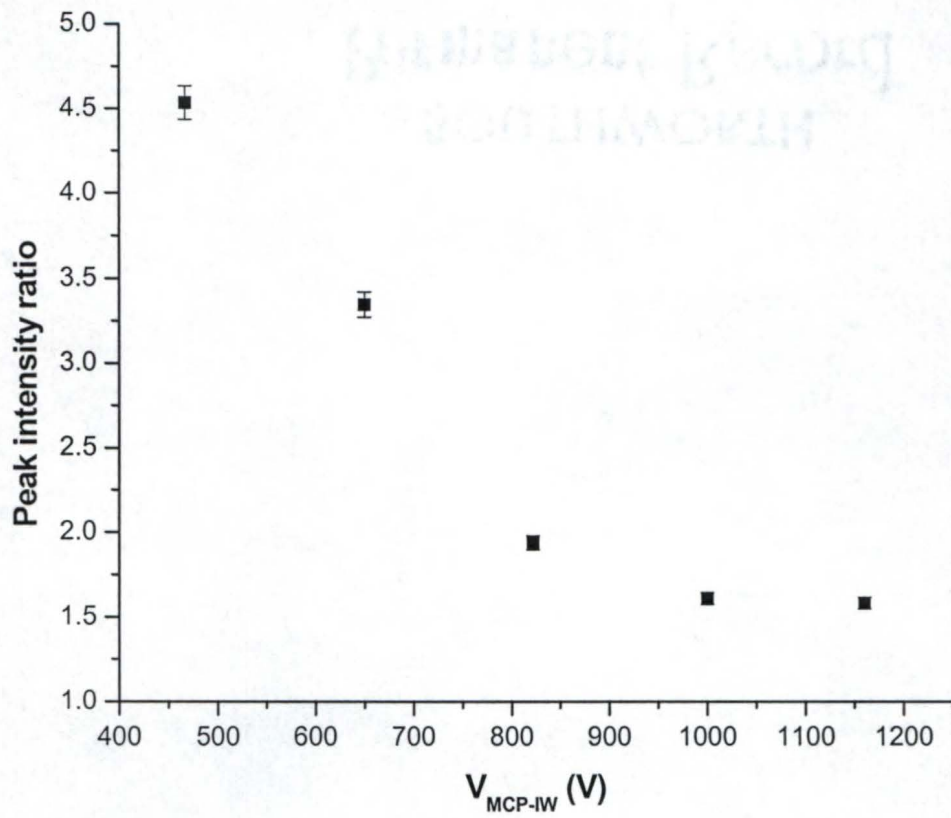


Figure 4-9. Peak intensity ratio as a function of V_{MCP-IW} .

expected, no signal component is detected. A different observation is made when λ_1 is present, but detuned away from the center of the absorption line. The PE signal remains constant, but the ionization signal components are reduced as λ_1 is tuned further away from the transition. Similar observations are made when λ_2 is eliminated or detuned. These data show that the unknown signal component is not formed via multiphoton ionization by the 435.8 nm photons of λ_2 or related processes. The unidentified signal is generated by some process involving 253.7 nm photons.

In summary, the identity of the ion responsible for the third non-imaging mode signal component remains unknown. The ion responsible is most likely positively charged and of low molecular weight. The ion is probably the result of some impurity introduced during cell construction. Possible impurities include sodium and potassium. Cell limitations did not allow the spectroscopic validation of these impurities.

CHAPTER 5 IMAGE DISTORTIONS IN THE RIID

The motivation behind the development of the RIID is the demand for a detector with the highest possible spectral resolution and 2-dimensional imaging capabilities. The current RIID design meets this demand and is capable of a spatial resolution of $< 80 \mu\text{m}$. As might be expected with any technology in the earliest stages of development, the RIID does have its share of limitations. The primary limitation for imaging mode RIID is image distortions [62]. Spatial resolution for a given experiment can be degraded over 2 orders of magnitude. An extensive investigation of these distortions and their origins provide insight toward the development of future RIID cells.

Overview of Image Distortions

In typical RIID experiments, an accelerating voltage is applied between the input window and microchannel plate, such that the positively charged mercury ions are accelerated toward the MCP for eventual detection. As a result of the polarity of the electric field, the electrons produced during ionization are accelerated toward the input window. After continuous periods of operation, charge may accumulate on the surface of the input window. The result of such surface charging is an altered electric field between the MCP and input window. The pathways followed by the ions traveling to the MCP are redirected and, in turn, the spatial distribution of the signal is altered. The redistribution of signal ions is observed experimentally as image distortions.

An improvement to the design of the RIID detectors, which eliminated this type of imaging artifact, has been previously reported [63]. This design enhancement involved

coating the inner surface of the input window with a thin palladium film. Although this metal film decreased the transmission of λ_1 through the input window by about 35%, image distortions were practically eliminated.

There are, however, observed limits to this improvement technique when implemented into the compact cell design discussed in this dissertation. Firstly, the non-uniformity of the metal film may allow different degrees of surface charging, or more likely, different rates of charge removal. Such film heterogeneity may allow variations in the electric field between the MCP and input window resulting in image distortions. Variations in metal film thickness may result from poor deposition methods or from highly energetic electron bombardment of the metal surface. Secondly, when high accelerating voltages are used, high energy electrons may pass through the metal film and penetrate into the quartz input window. The penetration depth of a high energy electron into a pure material of known density can be calculated by the empirical equation 5-1 [64,65].

$$D = \frac{0.1E_o^{1.5}}{\rho} \quad (5-1)$$

The penetration depth D is given in μm when E_o (kV) is the accelerating voltage experienced by the electron and ρ ($\text{g}\cdot\text{cm}^{-3}$) is the density of the material. This expression assumes a 5.0 mm distance between the stationary electron and surface. For a 10 nm thick Pd film under the given constraints for equation 5-1, an electron could penetrate the input window to a depth of 0.5 μm when $V_{\text{MCP-IW}} = 5\text{kV}$. Penetration of an electron into the quartz input window would result in the same type of electric field distortion, resulting in image distortions.

Experimental

The two color ionization scheme shown in figure 2-3 was employed in this study. $\lambda_1 = 253.7 \text{ nm}$ ($6^1S_0 \rightarrow 6^3P_1$) and $\lambda_2 = \lambda_3 = 435.8 \text{ nm}$ ($6^3P_1 \rightarrow 7^3S_1 \rightarrow \text{Hg}^+$) with measured pulse energies of $10 \mu\text{J}$ and $450 \mu\text{J}$, respectively, were used. It was shown that the behavior of the RIID, in terms of distortion effects, was unaffected when the three color ionization scheme in figure 2-3 was used.¹ A sheet of λ_2 and λ_3 was directed into the side window of the RIID approximately 0.25 cm from the input window.

Temporal Distortions

The intensity of the resonance ionization imaging signal under normal operating conditions should depend upon two experimental variables only. It is directly proportional to the pulse energies of the lasers and the magnitude of the applied voltages. However, it has been observed that under constant experimental conditions, image quality and intensity can vary with continuous operation. This is most readily observed when high $V_{\text{MCP-IW}}$ are applied. Typically, a voltage of 4.5–5.0 kV is applied between the MCP and input window for an optimal signal-to-noise ratio and spatial resolution. Nonetheless, these figures of merit are significantly impaired by image distortions with long operating times.

Figure 5-1 shows a typical series of images obtained as a function of time with $V_{\text{MCP-IW}} = 4.8 \text{ kV}$. The initial image ($t=0$) remains unchanged for approximately 6 minutes at which point image degradation is readily observed. For most applications, signal or image measurements would be made within this 6 minute window. For the

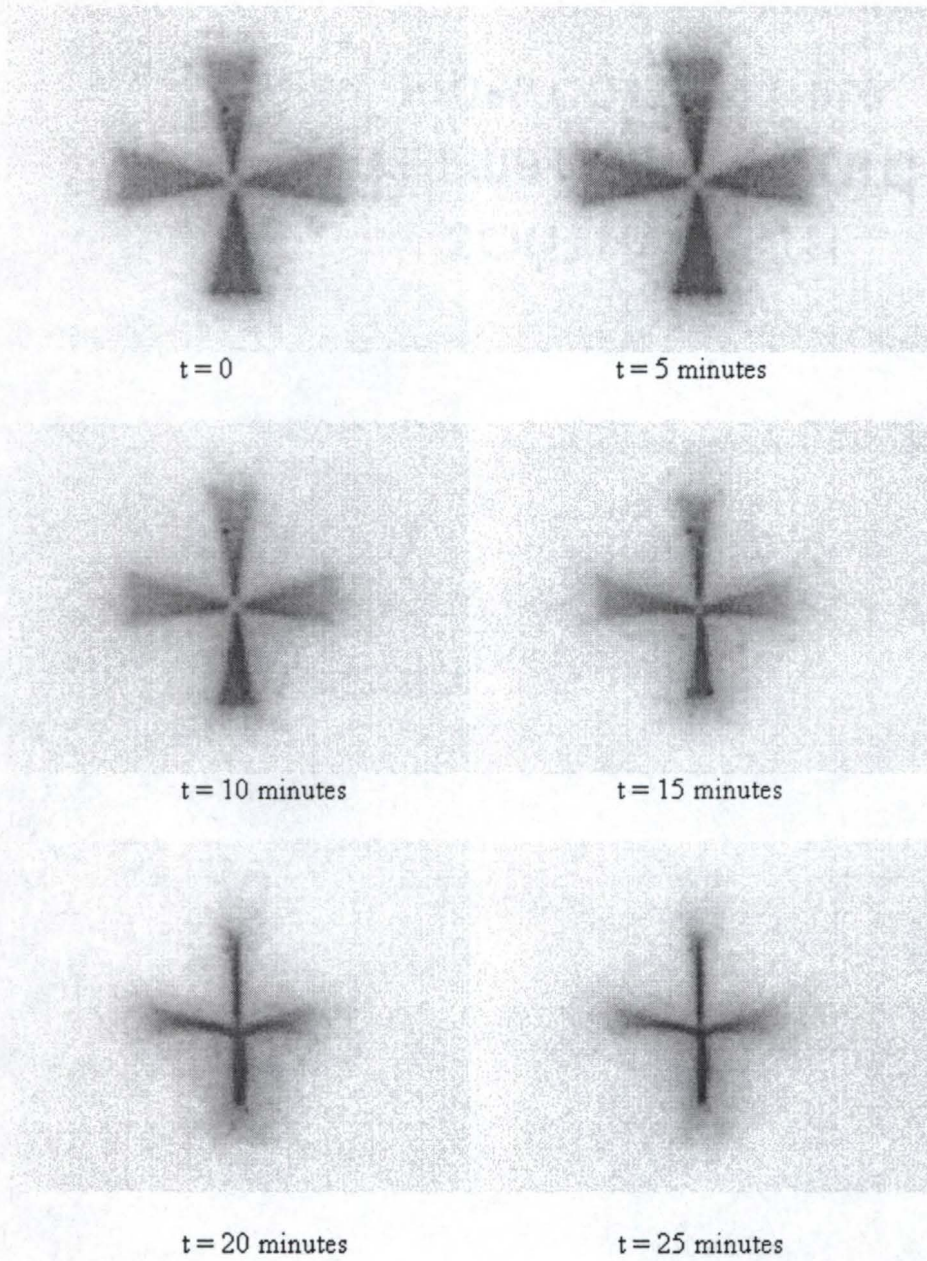


Figure 5-1. Image series with $V_{\text{MCP-IW}} = 4.8\text{kV}$.

detection of minimal λ_1 photons, when signal integration or image averaging is likely, this time frame may not be sufficient.

Cycling the power supply on and off upon the recognition of image artifacts does not recover the initial image. In fact, this distortion effect has been observed for several hours after the power supply has been shut off. It is implied from this data that some type of charging effect is involved. The charge will dissipate in most cases after 4-5 hours, at which point the image distortions are no longer observed.

Further proof of input window surface charging is realized when a "neutralization" potential is applied. By reversing the polarity of the electric field between the MCP and input window (i.e., *electron detection* mode which involves making the MCP more positive than the input window), image distortions are relieved within seconds rather than hours. Experimentally, this was accomplished by removing the input window from electric ground and connecting it within the 120 M Ω resistor chain shown in figure 2-6. There are two mechanisms by which the surface charging is relieved in this case. The first mechanism involves the acceleration of the accumulated electrons away from the input window (toward to the MCP). A second possible mechanism is the neutralization of the negative charge by positively charged mercury ions as they are then accelerated toward the input window. A combination of these mechanisms is most likely. The duration of this reversed field is on the order of 1-2 seconds. Experimental limitations prevent an accurate measurement of the reversed field duration. Experimental limitations also prevent signal measurements, imaging or non-imaging, during this period.

As discussed above, the purpose of the metal film coating on the input window, when connected to electrical ground, was to minimize the accumulation of charge. A possible

limitation of the metal film is realized when high energy electrons pass through the film and are accumulated between the film and window. When the kinetic energy of the electron is great enough, penetration into the window could occur. This possibility was evaluated by collecting images with a lower V_{MCP-IW} . As is shown in figure 5-2, image distortions are not observed when a lower V_{MCP-IW} (1.0 kV), than in the previous example, is applied. Equation 5-1 above supports these experiments. From equation 5-1, it was calculated that an electron would not have sufficient energy to travel through the thin metal film. A minimum V_{MCP-IW} for electron penetration through the metal film was estimated to be 1.64 kV. These data imply that the distortions shown in figure 5-1 are a result of high energy electrons passing through the metal film, thus voiding its benefit.

It should be noted that the S/N and spatial resolution of the initial image ($t=0$) are degraded here compared to the previous example. However, they do remain constant through the duration of the experiment. Decreased S/N and spatial resolution at lower, non-optimized voltages as expected. The spatial resolution obtained for both low and high voltage experiments is shown graphically in figure 5-3. It is shown here that spatial resolution is not compromised by temporal distortions for the low voltage experiments. The spatial resolution is not optimal, but does remain constant for the duration of the experiment. The distortion effect for the higher voltage experiments, as a function of time, is linear. A distortion rate constant (r) of $38 \mu\text{m}\cdot\text{min}^{-1}$ is obtained for the high voltage experiments. This constant was obtained from the slope of the of the curve

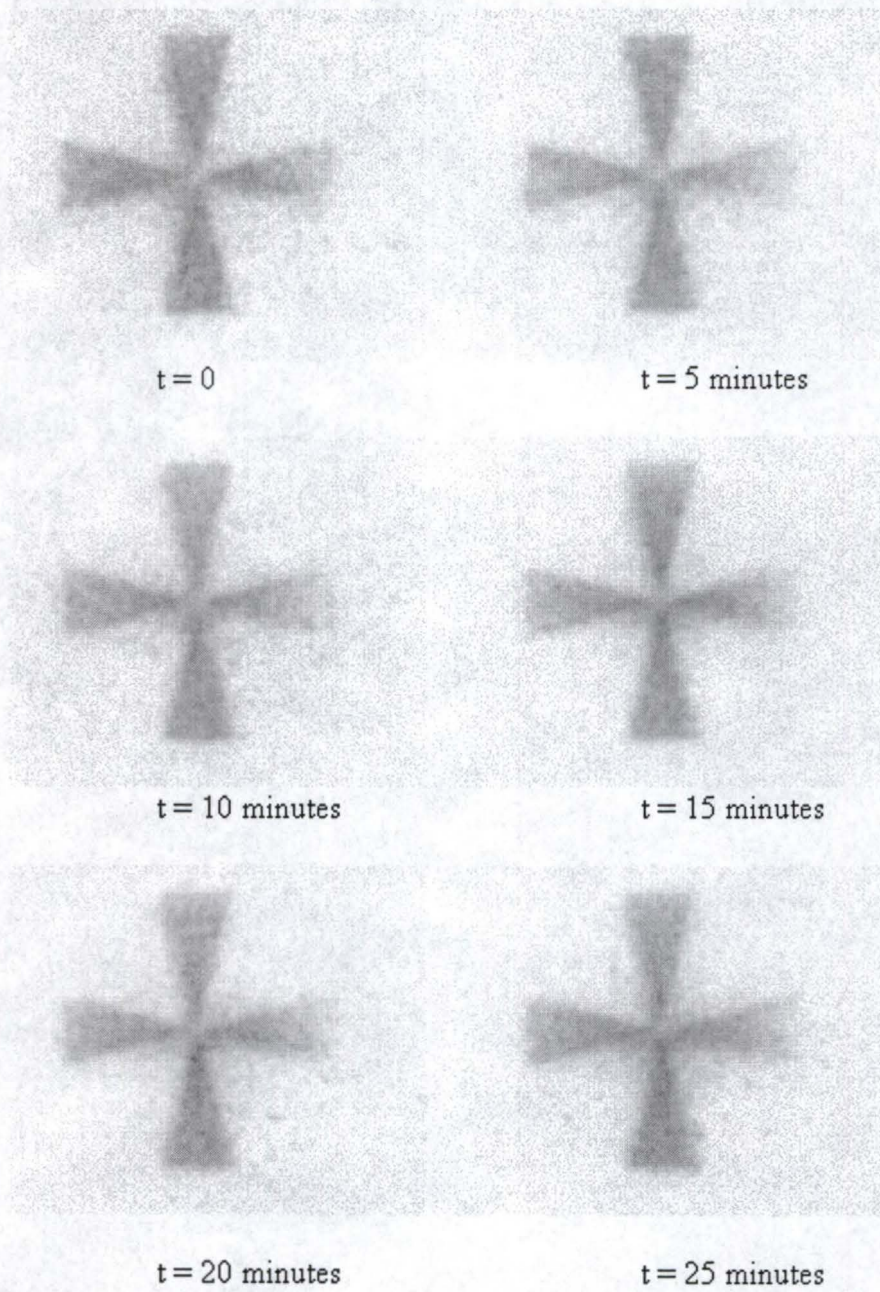


Figure 5-2. Image series with $V_{\text{MCP-IW}} = 1.0\text{kV}$.

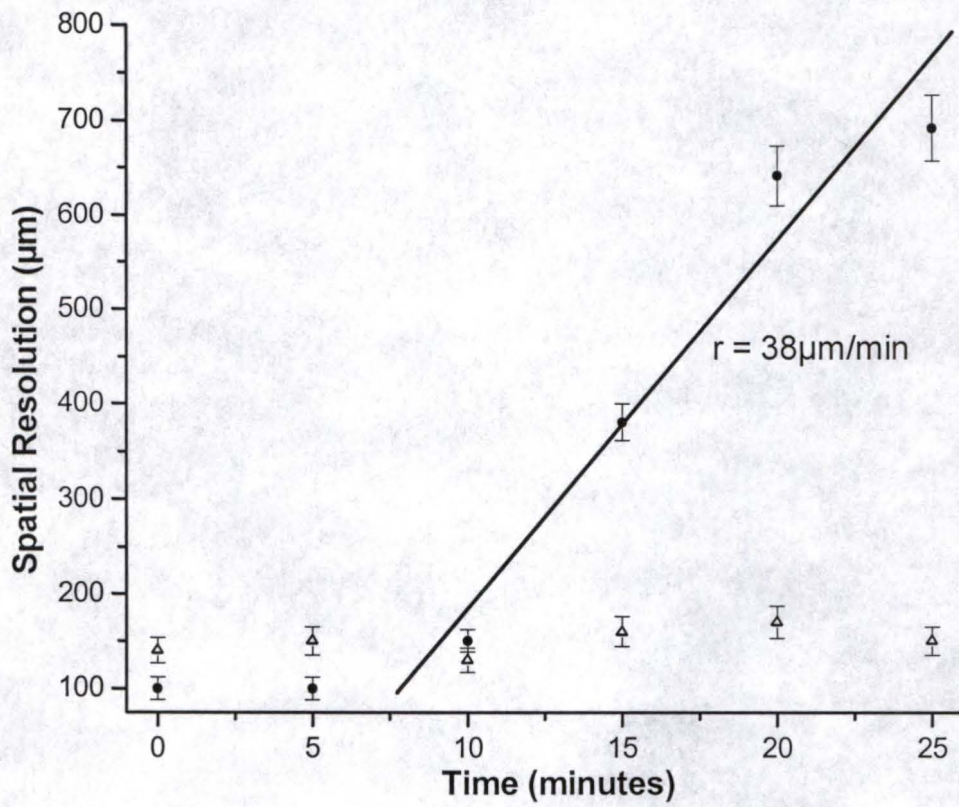


Figure 5-3. Spatial Resolution as a function of time. \bullet - $V_{\text{MCP-IW}} = 4.8 \text{ kV}$; Δ - $V_{\text{MCP-IW}} = 1.0 \text{ kV}$.

shown in figure 5-3. As discussed above, and as shown in figure 5-3, that $r = 0$ for up to 10 minutes of continuous operation.

Input λ_1 photons are distributed in the shape of an imaged object or, in the this work, as the shape of an imaging mask. Under ideal conditions, ionization will occur in a like arrangement and eventual signal detection will follow as such. When the electric field between the MCP and input window is altered, this ideal situation is not observed. The image distortions shown in figure 5-1 are the result of the signal "redistribution" in the atom cell. Although altered pathways occur between the ionization region and the MCP, each ion generated in the atom cell is still detected. The proof of this signal conservation during image distortions can be illustrated when the RIID is simultaneously operated in both imaging and non-imaging modes. Figure 5-4 shows that the magnitude of the resonance ionization signal remains constant during distortion conditions. Less than 5 % difference was measured for non-imaging mode signals measured at 2 and 20 minutes.

In summary, it is shown that conditions for optimal image S/N and spatial resolution in the RIID may result in severe image distortions. These distortions occur when the RIID is operated at high V_{MCP-IW} for extended periods of time.

Relief of imaging distortions is possible by allowing the charge to naturally dissipate with time, which can require up to 6 several hours. Almost instant distortion relief is possible with the application of a neutralization potential (V_{MCP-IW}). Furthermore, distortions may be prevented completely by operating the RIID at lowered voltages. However, the elimination of distortions in this fashion are at the expense of image S/N and spatial resolution.

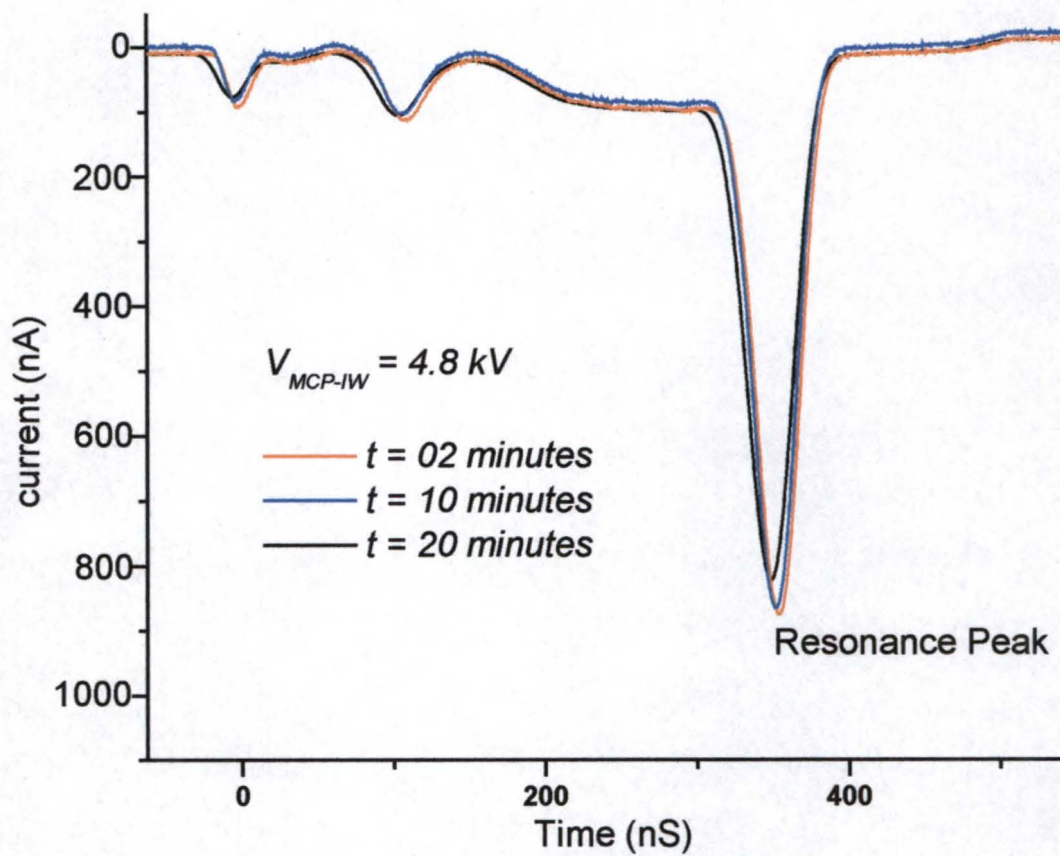


Figure 5-4. Signal conservation during image distortions.

Other methods to minimize, or even prevent, these imaging distortions are possible. One such method would be to employ lower repetition rate lasers and, thus, less frequent image acquisitions. In such a fashion, the ion/electron pair would be created less frequently and the rate of charge accumulation would be reduced or even prevented. A second method might incorporate electronics to alternate the system between ion and electron detection modes. Since image distortions occur after about 6 minutes of continuous operation, the mode switching frequency should be on the order of about 3 mHz. In this case, the accumulated charge would be "neutralized" before image distortions occurred.

Spatial Distortions

Image distortions can also be observed with high levels of incident λ_1 photons and low voltages, when the position of λ_2 and λ_3 in the side window is varied. This type of imaging artifact results only from λ_2 and λ_3 position and not the extent of the operational period. Figure 4-2 illustrates the variable position of λ_2 and λ_3 in the side window of the RIID. When the sheet of λ_2 and λ_3 light is brought relatively close to the input window, within 2.0 mm, *short term* distortions occur. In other words, λ_2 and λ_3 can be moved back into their original positions without prolonged image distortions. Figure 5-5 shows such distortions as a result of the position of λ_2 and λ_3 . The results here are consistent with those discussed in the case of temporal distortions. By moving the ionization region close to the input window, a dense region of electrons is created close to the input window. Consequently, the electric field between the input window and the MCP is altered and image distortions are observed. However, unlike the temporal

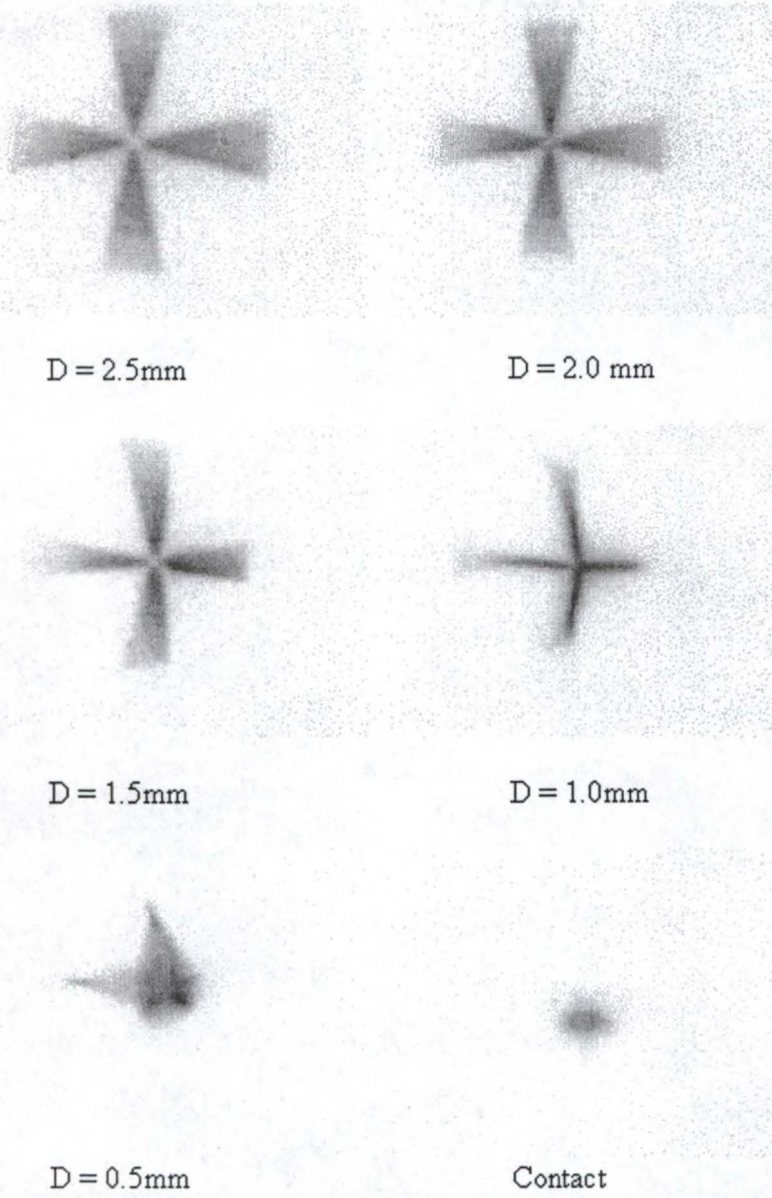


Figure 5-5. Spatial image distortions in the RIID.

distortions discussed above, this case is reversible. Simply moving the ionization region away from the input window minimizes these imaging distortions.

CHAPTER 6 POTENTIAL APPLICATIONS

There are numerous potential applications that exist for the resonance ionization imaging detector because of its high spectral resolution and sensitivity. These applications are most numerous throughout the fields of analytical science, such as plasma diagnostics, ion mobility spectrometry, Raman spectrometry, and particle size distribution measurements for combustion analysis. Other possibilities include combustion product imaging, aerodynamic field flow imaging, ultrasonic field imaging, as well as a host of biomedical, military, and atmospheric applications. Of particular interest is the application of moving object detection. Almost any type of moving object could, in theory, be studied with the RIID: combustion products in flames, aerodynamic flow fields, and even macroscopic projectiles. Figure 6-1 depicts a general experimental setup that might be used for such applications.

Moving Object Detection

The premise behind moving object detection is that λ_1 , detuned from the resonance line, will illuminate a moving object and be scattered back to the RIID. Detection of the moving object will occur when the scattered illuminating frequency is Doppler shifted back into resonance with the mercury. A similar application might involve a molecule shifting λ_1 back into resonance with mercury via a Raman shift. Although conventional imaging systems are capable of detecting the rather large shifts associated with the Raman effect, the high sensitivity of the RIID could improve Raman imaging techniques.

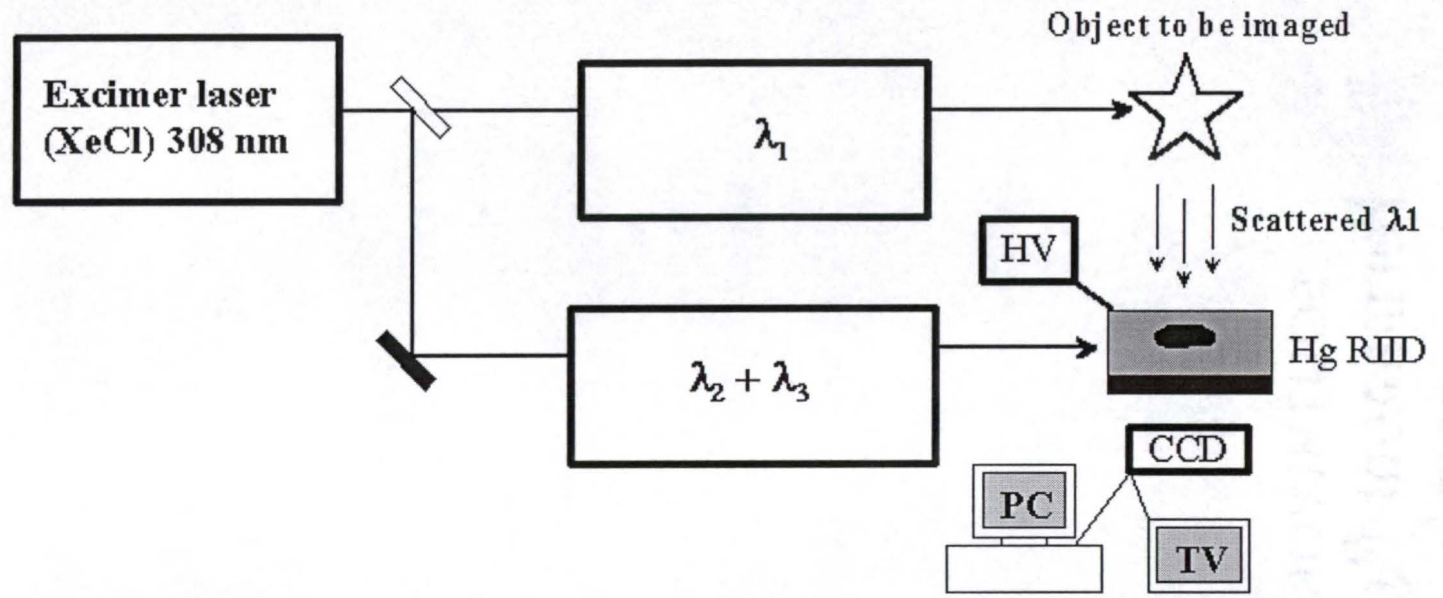


Figure 6-1. Experimental setup for RIID applications.

Monte Carlo Simulation of Moving Object Detection

Jelalian has previously described the detection of moving objects upon the earth's surface with laser radar techniques [66]. This was achieved when the background scattering radiation was practically eliminated using coherent laser radar, which itself is considered a scanning imaging technique [67]. Comparatively, the RIID could detect these moving objects with greater speed and with much more valuable target recognition information without scanning. The following summary of this Monte Carlo simulation (MCS) study will show that the UBID should be an extremely sensitive detector for a variety of moving objects in turbid media.

The Monte Carlo program used in this study was developed at St. Petersburg University, Russia. The model, upon which the program is designed, consists of four planes and is defined as the following: the plane of the moving disk, the plane of the turbid media surface, the plane of the lens, and the RIID plane, as depicted in figure 6-2. The distance between the lens and the medium surface is equal to the distance between the lens and the RIID. Scattering is assumed to be isotropic in the plane perpendicular to photon propagation and distributed in accordance with Henyey–Greenstein relationships [68]. When a photon is scattered from the moving disc, a Doppler shift occurs. The variable parameters of this simulation software are defined in table 6-1. All calculations are performed in the photon's system of coordinates. In the beginning of every elementary action, a random path length (L_R) for each photon generated. This length is then compared with $1/\mu_{\text{abs}}$ and $1/\mu_{\text{scat}}$. The photon is considered to be "alive", or still propagating, if $L_R < 1/\mu_{\text{abs}}$. This same photon, of path length L_R , can undergo scattering

Variable	Default value	Definition
α_{inc}	90.0°	Angle of incidence of laser beam with respect to the plane of the medium surface.
v_{disc}	30 m·sec ⁻¹	Disk velocity
v_{center}	2580 x 10 ⁻⁶ cm ⁻¹	The spectroscopic shift of the illuminating laser radiation.
μ_{scat}	0.50 mm ⁻¹	Scattering coefficient; scattering centers per unit length.
R_{disc}	10 mm	Disk radius.
$N_{photons}$	10 ⁶	Initial number of photons.
Focus	30 mm	Focal length of lens.
k_{aver}	10 cm ⁻¹	Absorption coefficient of the RIID.
λ_{laser}	760 nm	Wavelength of incident radiation.
g_a	0.5	Anisotropy factor.
l_{RIID}	-	Random path length in RIID.
L	1.0 mm	Depth of disk in turbid medium.
L_R	-	Random path length in turbid medium.
μ_{abs}	0.50 mm ⁻¹	Absorption coefficient; absorbing centers per unit length.
δv	100.00 x 10 ⁻⁶ cm ⁻¹	Spectroscopic absorption range of the RIID.
D_{laser}	30.0 mm	Diameter of the laser beam.
N_{acts}	9000	Number of scattering events per photon.
Radius	20.0 mm	Radius of lens.
$RIID_{width}$	1.0 cm	Width of the RIID.

Table 6-1. MCS software variable definitions and default values.

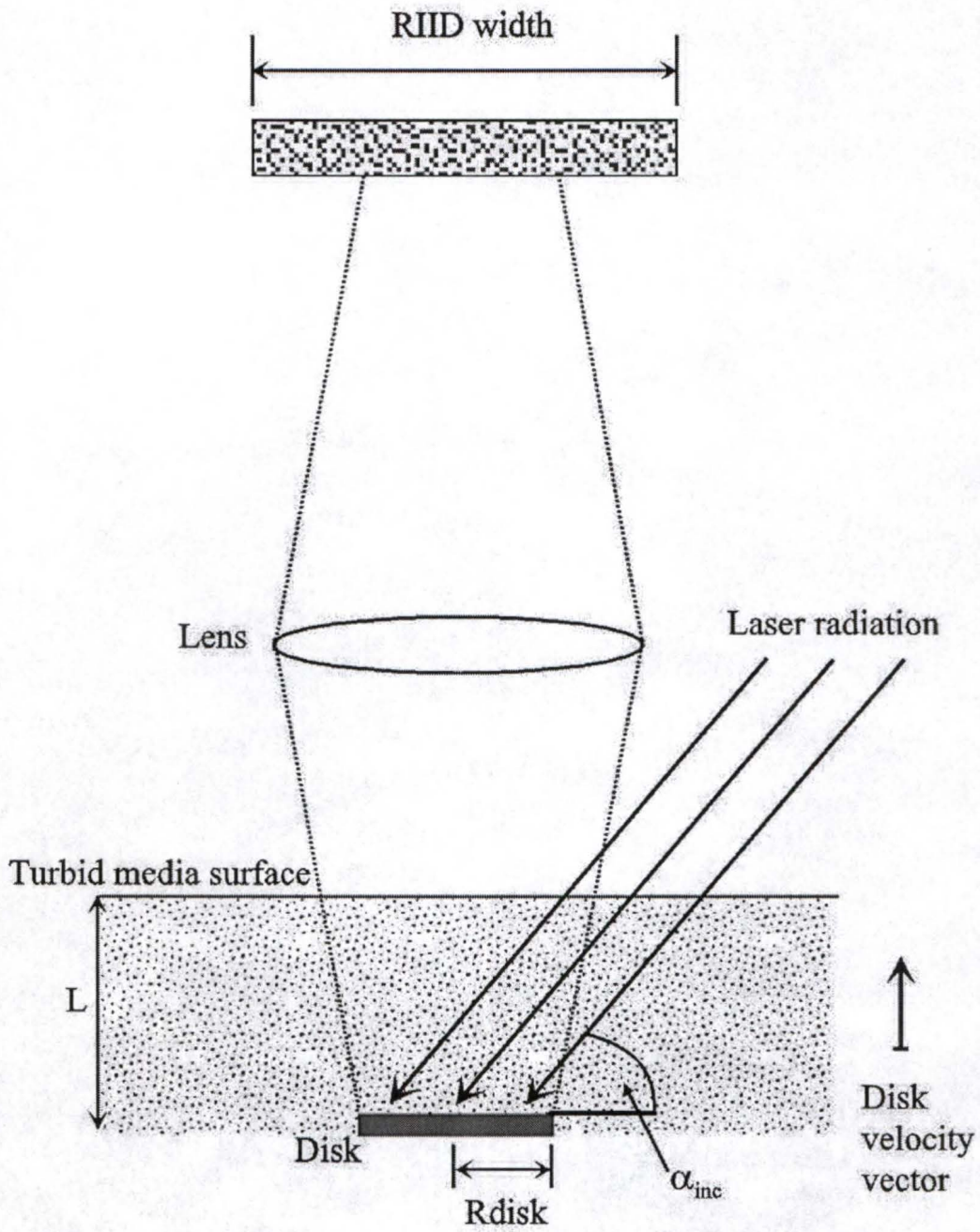


Figure 6-2. Schematic diagram of MCS model.

events if $L_R > 1/\mu_{\text{scat}}$. If $L_R < 2L \sin(\alpha_{\text{inc}})$, then the photon is randomly scattered from the disc and away from the medium. At this point the photon can be detected by the RIID if, of course, the angle at which it is leaving is within the field of view of the lens. This is shown graphically in figure 6-2. Angle coordinates of this photon are then recalculated to obtain the final coordinates of the photon upon the RIID surface. The resulting image is that of the disk. The photons which remain active, but within the turbid medium, can again be scattered or absorbed. In principle, a photon can collide with the disc and scattering particles several times. In this case, the linewidth of the scattered radiation will be much greater than laser spectral linewidth. For every photon that reaches the RIID, the random path length (l_{RIID}) is generated and then compared with the existing RIID width. If $l_{\text{RIID}} < \text{RIID}_{\text{width}}$ a photon is considered to be detected.

For simplicity, these simulations were performed for short distances between the moving object and RIID and for a laser wavelength of 760 nm. If desired, these simulations could be applied to long distances as well. However, there will be more photons which "die" or are scattered away from the detector over a larger distance. To compensate for this, the number of initially emitted photons should be increased. A value of 9000 for N_{acts} was selected after the realization that higher values do not render any noticeable changes.

The first simulation, shown in figure 6-3, shows the MCS image of a stationary object in a turbid medium with small scattering and absorption coefficients. No distinct features are revealed from this image for two reasons. In this first simulation, the MCS parameter for v_{center} is zero. This implies that a Doppler-shifted frequency from any

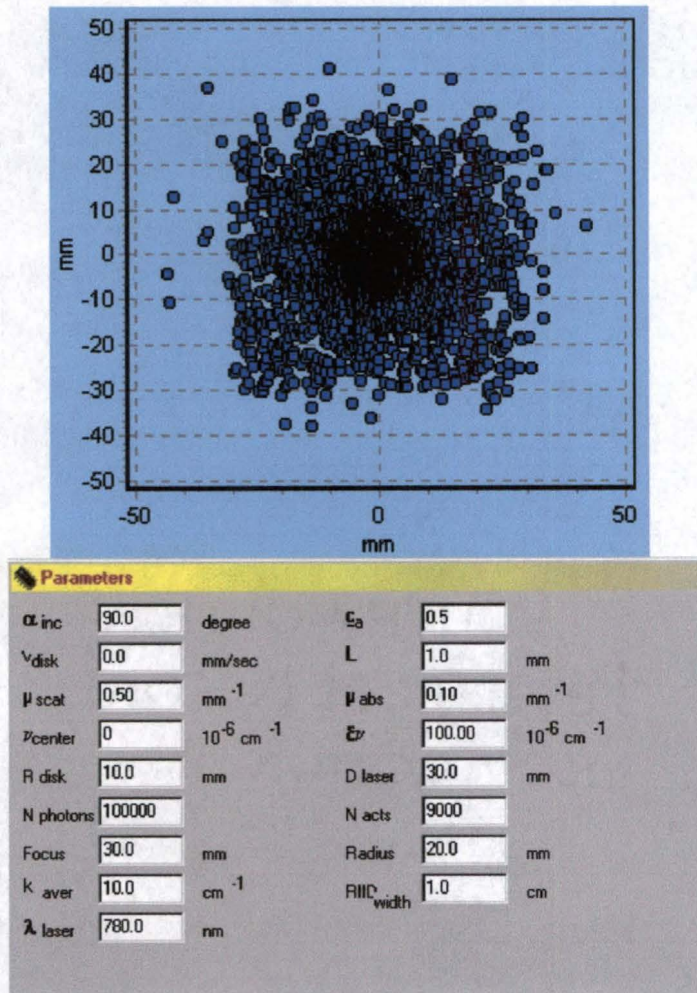


Figure 6-3. Simulation with $V_{disk} = 0$ m/s and $v_{center} = 0$

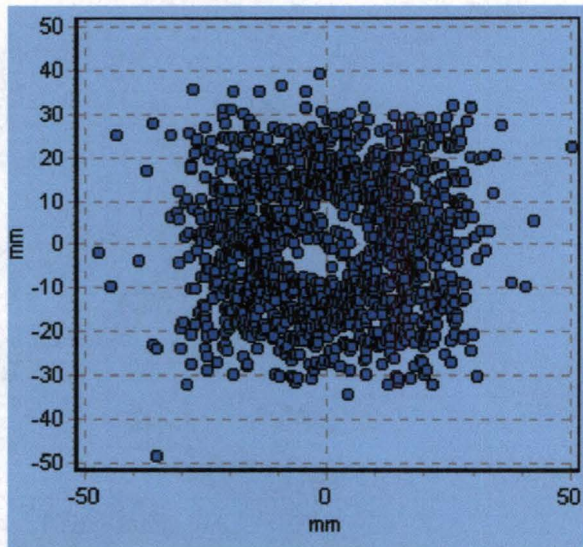
moving object was present, namely the disk or medium, it would not have been detected. Secondly, and more obvious, the disk velocity in this example is zero. Regardless of the v_{center} parameter value, a stationary disk would not produce a Doppler-shifted frequency. In summary, a scattering object is detected, but cannot be resolved. This example might represent the image of a stationary object by a conventional detection system.

The parameters in simulation 2 are identical to those in the previous simulation, except that the disk velocity is 30.0 m/s rather than 0. Again, there is no recognizable object in the MCS image shown in figure 6-4. However, one significant change is observed from the first simulation. The number of photons detected is greatly reduced. Also, there is a vacancy of signal from the center of the image in the form of a disk. Such a result is considered a “negative” image. This image arises from the Doppler shift of the moving disk and $v_{center} = 0$.

When the shift parameter v_{center} is changed to the predicted value of the Doppler shift, as shown in simulation 3, complete “resolution” of the moving disk is observed (figure 6-5). Resolution in this context refers to the unmistakable shape of the image and its observed diameter, and should not be confused with resolution as an analytical figure of merit. The spectroscopic shift parameter, v_{center} , is easily calculated from the Doppler equations for a disk of known velocity.

$$v_{center} = -(2v_{disk} / \lambda_{laser}) \sin(\alpha_{inc} / 2) \quad (6-1)$$

As one might anticipate from the direct proportionality of this equation, a larger disk velocity results in a relatively large spectroscopic shift from the center of the incident



Parameters				
α inc	90.0	degree	c_a	0.5
v_{disk}	30000.0	mm/sec	L	1.0 mm
μ scat	0.50	mm ⁻¹	μ abs	0.10 mm ⁻¹
ν_{center}	0.00	10 ⁻⁶ cm ⁻¹	ϵ_{ν}	100.00 10 ⁻⁶ cm ⁻¹
R disk	10.0	mm	D laser	30.0 mm
N photons	100000		N acts	9000
Focus	30.0	mm	Radius	20.0 mm
k aver	10.0	cm ⁻¹	RIIC width	1.0 cm
λ laser	780.0	nm		

Figure 6-4. Simulation with $v_{\text{disk}} = 30.0\text{m/s}$ and $v_{\text{center}} = 0$

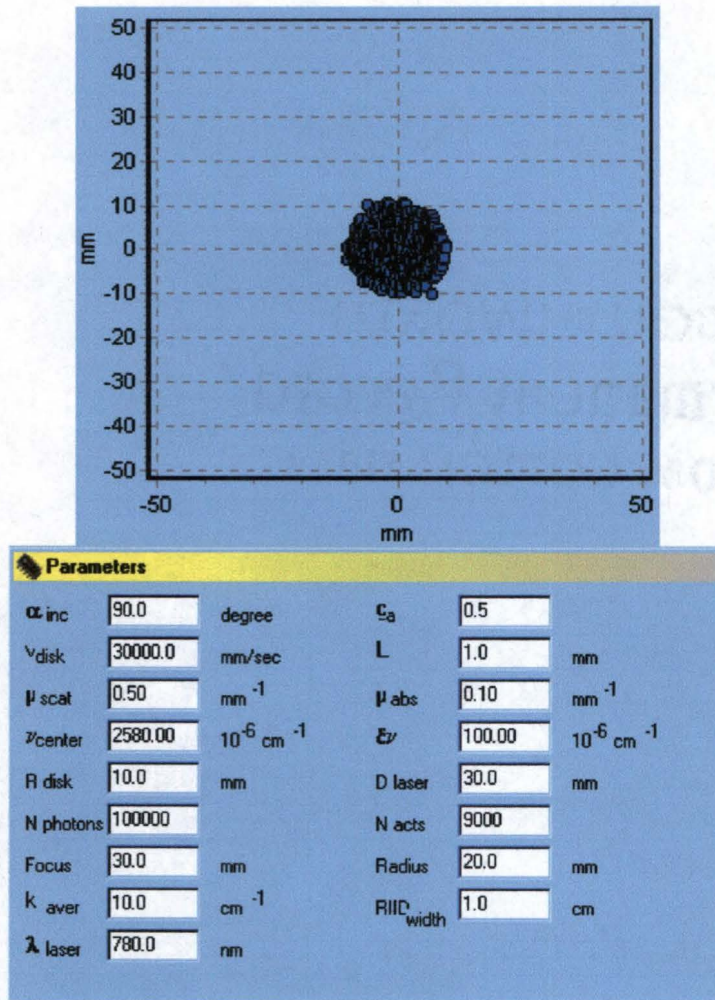


Figure 6-5. Simulation with $v_{\text{disk}} = 30.0\text{m/s}$ and $v_{\text{center}} = 2580 \times 10^{-6} \text{ cm}^{-1}$

laser frequency. Larger velocities will allow better resolution of the irradiating and Doppler shifted frequencies. Conversely, this also implies that some minimum disk velocity exists at which these frequencies can no longer be resolved. Figure 6-6 illustrates both of these implications. Shown here are signal profiles across the RIID detection range at two different disk velocities. Except for v_{center} and V_{disk} , MCS conditions are identical to those in simulation 3. The signal maxima are resolved in both cases, but a lower disk velocity limit for baseline resolution is about 2 m/s is realized. The shifted profile width remains constant over an extended disk velocity range. The peak width was studied as a function of several other factors, including μ_{scat} and μ_{abs} . In all cases, the peak width appeared to remain constant (within 5%). In highly absorbing and scattering media (high μ_{abs} and μ_{scat}), the total number of detected photons is greatly reduced. In simulation 1, several hundred photons are shown to be detected. As is the case in simulation 4, shown in figure 6-7, fewer than 20 photons are detected when μ_{scat} is increased.

The image in simulation 4 has become less indicative of the shape of the moving object. From such an image, one could not conclude that the object is a disk; only that it is an object with a velocity of 30.0 m/s. This type of detection without identification becomes more prevalent as various parameters (such as μ_{scat}) are increased and, in turn, the number of detected photons are decreased. For example, it has been shown that a moving object can be detected with a scattering coefficient greater than 30 mm^{-1} . This is comparable to the results described by Soelkner.¹⁰ In such an example, the detected number of photons may be as few as one or two, which is an indication that a moving object is present. The Doppler shift exhibited by the detected photons, as few as there

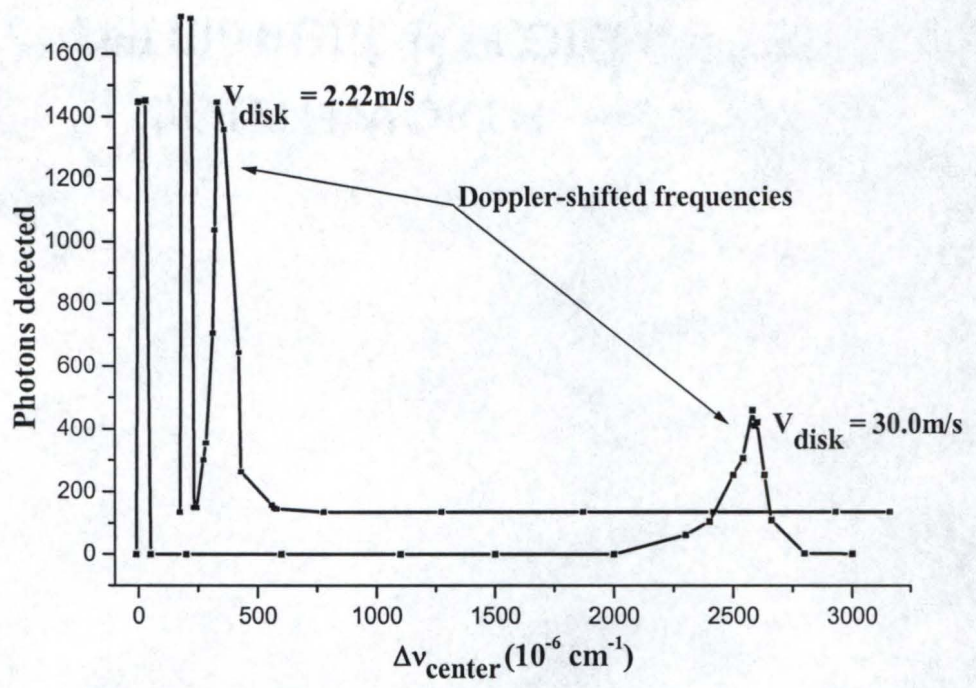


Figure 6-6. Doppler shifted profiles.

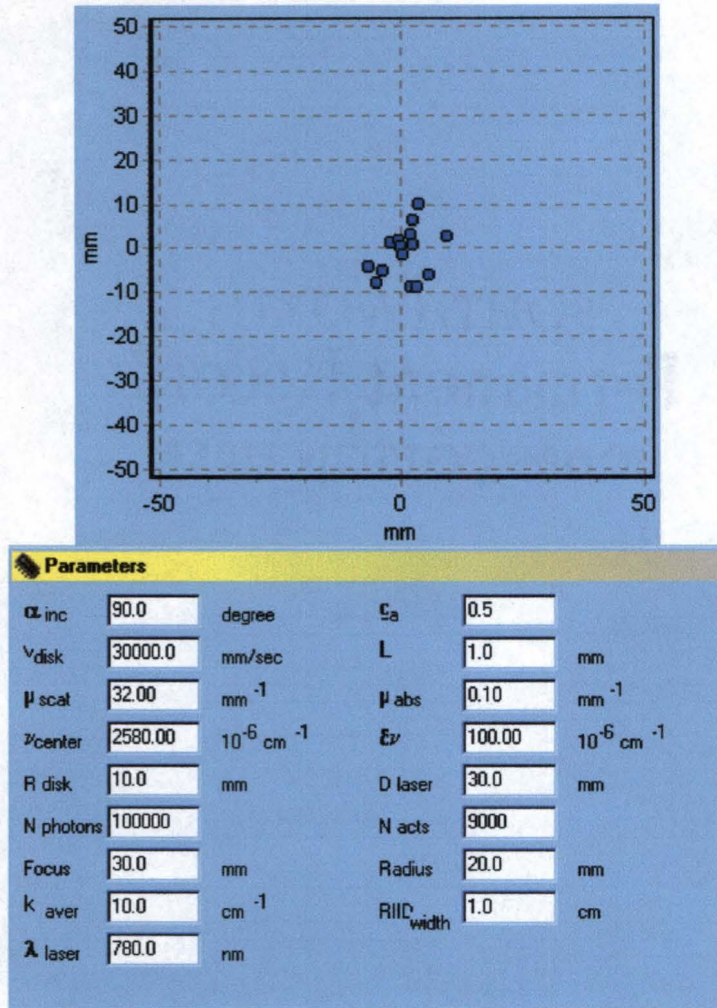


Figure 6-7. Simulation with $v_{\text{disk}} = 30.0\text{m/s}$, $v_{\text{center}} = 2580 \times 10^{-6} \text{ cm}^{-1}$, and $\mu_{\text{scat}} = 32.0 \text{ mm}^{-1}$

might be, must be induced by a moving object. Simulation 5, shown in figure 6-8, further illustrates this as a moving object is detected when both μ_{scat} and μ_{abs} are increased.

To further demonstrate the utility of this RIID model, several of the above simulations were repeated for mercury at the 253.7 nm transition. The velocity of the object (disk) was increased to 300 m/s and the spectroscopic linewidth was increased to 1 GHz. The behavior was nearly identical or comparable to the 760 nm study. The ratio of detected photons at $\nu_{\text{center}} = 2.3 \text{ GHz}$ (0.0788 cm^{-1}) to the detected photons at $\nu_{\text{center}} = 0$, or signal to background ratio, is 2.4×10^{-4} . Nevertheless, this mathematical model and simulation shows that the moving target is clearly detected. It is important to emphasize here that identification and detection are unique figures of merit.

It is necessary to note the limitations and/or restrictions of the MCS program and the differences between real and simulated moving object detection. The actual spectral line-shape of a RIID is not rectangular, but normally Gaussian or Lorentzian. Illumination of a moving object by laser radiation is much more complicated than described here. Homogenous and isotropic scattered light is not produced from the surface of the moving object. Actual distances between the RIID and the moving object would be much larger than in these simulations. The default number of scattering events ($N_{\text{acts}} = 9000$) can be much larger. The distance choice here was made for simplification and shorter calculation times.

In summary, we have shown that the detection and identification of moving objects in turbid media with a RIID is theoretically possible. All of the results thus far are promising for the future development of such an imaging device. The model employed here is limited only by the number of photons which can penetrate the turbid

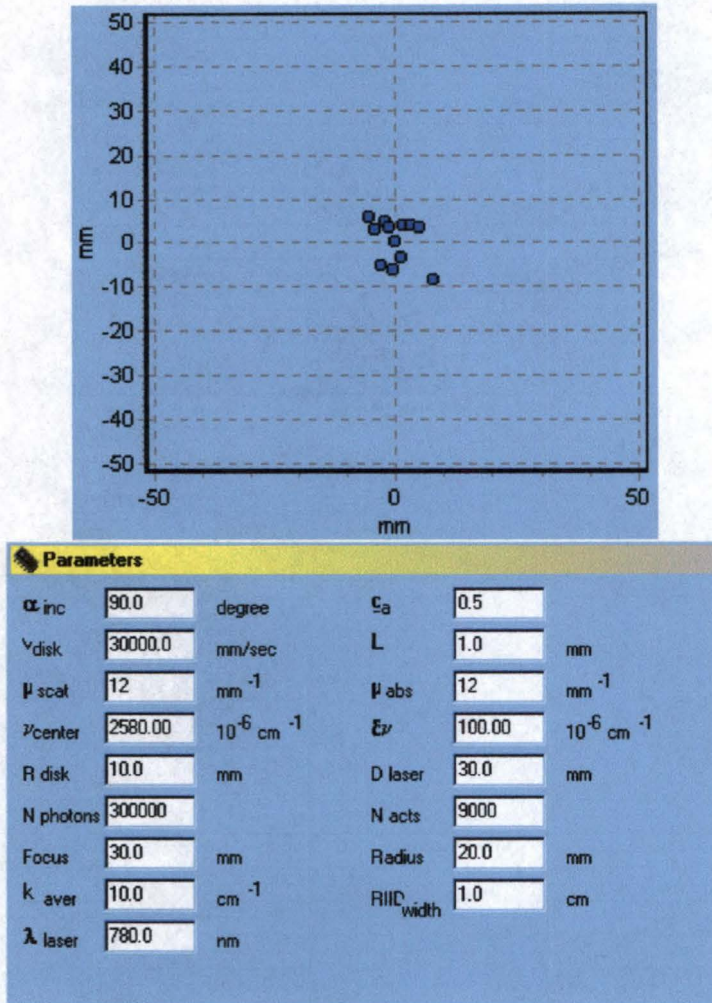


Figure 6-8. Simulation with $V_{disk} = 30.0\text{m/s}$, $\nu_{center} = 2580 \times 10^{-6} \text{ cm}^{-1}$, $\mu_{scat} = \mu_{abs} = 12.0 \text{ mm}^{-1}$

medium. It has been demonstrated that a moving object can be detected in a medium where the scattering coefficient is greater than 35 mm^{-1} .

The model of moving object detection in turbid media described in this chapter could be demonstrated in several types of experiments. A particular combustion product, with velocity related to its size, could be imaged in the presence of various other scattering and absorbing particles [69]. This could provide some insight into particle formation in various types of flame or engines. Another application, represented by the preceding simulations, could be realized by the military for imaging projectiles in the atmosphere. A bullet or missile in the atmosphere could be imaged with overcast conditions, providing both velocity and structural information.

CHAPTER 7 FINAL COMMENTS

Conclusions

The mercury resonance ionization imaging detector has previously been demonstrated as sensitive and spectrally selective photon detector. In this work, a compact and self-contained Hg RIID was effectively demonstrated. This RIID was shown to be capable of detecting fewer than 10^3 photons at 253.7 nm in non-imaging mode. When operated in imaging mode, the RIID described here is capable of spatial resolutions less than 80 μm .

As with the development of any novel technology, the RIID discussed here has several limitations. The primary limitation of this Hg RIID is that it's susceptible to image distortions. Several methods have been suggested to prevent, minimize, or even eliminate these distortions. Also, the capabilities of the RIID as a 1-dimensional photon detector are not limited by these distortions. Non-imaging mode experiments verify that, although spatially redistributed, the signal ions are detected.

Future Work

The priority for improvements to the mercury RIID is engineering quality control. The RIID described in this work was hampered from several unknown material specifications. These included the actual MCP amplification factor, the true thickness of the phosphor screen and metal films, the composition of the mercury dispenser, the exact pressure within the cell, and the quantum efficiency of the phosphor screen. A knowledge of several of these specifications might provide some insight into the unknown ionization component discussed in chapter 3.

As a method to eliminate surface charging effects, and hence image distortions, a thicker and more uniform Pd film should be coated on the input window. The result would be a more homogenous electric field between the input window and MCP. Also, the photoelectrons would be grounded instead of penetrating into or accumulating upon the surface of quartz window. Not only would the image distortions be prevented, but the spatial resolution might be improved upon.

The spectral resolution of the detector in this study is defined as the absorption linewidth of the contained mercury vapor. Replacing this isotopic mixture with a monoisotopic atomic vapor, such as ^{202}Hg , would improve the spectral resolution of the RIID to about 1 GHz. This would aid in such applications as moving object detection.

Work has already begun to employ the RIID for several of the previously mentioned applications including moving object detection and Raman imaging. To aid in the successfulness of these experiments, construction has begun on a tunable and ultra-narrowband Alexandrite laser system. In addition to the improved spectral resolution obtainable with this new laser, the overall size of the experimental setup will be reduced by 4-5 times.

LIST OF REFERENCES

- [1] O. Matveev, B. Smith, J. Winefordner, *Applied Optics* 36 (1997) 8833.
- [2] O. Matveev, B. Smith, J. Winefordner, *Applied Physics Letters* 72 (1998) 1673.
- [3] O. Matveev, B. Smith, J. Winefordner, *Optics Letters* 23 (1998) 304.
- [4] O. Matveev, B. Smith, J. Winefordner, *Optics Communications* 156 (1998) 259.
- [5] O. Matveev, *Zhurnal Prikladnoy Spektroskopii* 46 (1987) 359.
- [6] R. Miles, W. Lempert, *Applied Physics B* 51 (1990) 1.
- [7] M. Smith, G. Northam, J. Drummond, *AIAA* 34 (1996) 434.
- [8] N. Finkelstein, W. Lempert, R. Miles, *Optics Letters* 22 (1997) 537.
- [9] D. Skoog, J. Leary, *Principles of Instrumental Analysis*, 4th ed, Saunders College Publishing, Philadelphia, 1992.
- [10] D. Pappas, O. Matveev, B. Smith, M. Shepard, A. Podshivalov, J. Winefordner, *Applied Optics* 39 (2000) 4911.
- [11] V. Letokhov, *Laser Photoionization Spectroscopy*, Academic Press, New York, 1987.
- [12] G. Magerl, B. Oehry, W. Ehrlich-Schupita, *Institut für Nachrichtentechnik und Hochfrequenztechnik, Conference Proceedings*, Vienna, 1991.
- [13] R. Ambartsumian, V. Kalinin, V. Letokhov, *Pis'ma Zhurnalu Eksperimental'noy i Teoreticheskoy Fiziki* 13 (1971) 305.
- [14] G. Hurst, M. Payne, *Principles and Applications of Resonance Ionization Spectroscopy*, Adam Hilger Publishers, Bristol, TN 1988.

- [15] G. Hurst, M. Nayfeh, J. Young, *Applied Physics Letters* 30 (1977) 229.
- [16] G. Bekov, V. Letokhov, O. Matveev, V. Mishin, *Pis'ma Zhurnalu Eksperimental'noy i Teoreticheskoy Fiziki* 28 (1978) 308.
- [17] U. Brinkman, W. Hartwig, H. Telle, H. Walther, *Applied Physics* 5 (1974) 109.
- [18] D. Skoog, F. Holler, T. Nieman, *Principles of Instrumental Analysis*, 5th ed, Saunders College Publishing, Philadelphia, 1998.
- [19] V. Antonov, I. Knyazev, V. Letokhov, V. Matiuk, V. Movshev, *Pis'ma Zhurnalu Eksperimental'noy i Teoreticheskoy Fiziki* 3 (1977) 1287.
- [20] L. Zandee, R. Bernstein, *Journal of Chemical Physics* 71 (1979) 1359.
- [21] S. Rockwood, J. Reilly, K. Hohla, K. Kompa, *Optics Communications* 28 (1979) 175.
- [22] N. Omenetto, *Journal of Analytical Atomic Spectrometry* 13 (1998) 385.
- [23] O. Matveev, B. Smith, N. Omenetto, J. Winefordner, *Spectrochimica Acta B* 51 (1996) 563.
- [24] M. Shepard and J. Winefordner, *Microscopy and Analysis* (2000) 19.
- [25] O. Matveev, B. Smith, N. Omenetto, J. Winefordner, *Applied Spectroscopy* 53 (1999) 1341.
- [26] SAES Getters Incorporated, Getter-type Mercury Dispenser Products, http://www.saesgetters.com/prdfr_mdiss.htm, December 2001.
- [27] O. Matveev, N. Omenetto, *Resonance Ionization Symposium Conference Proceedings*, American Institute of Physics, 1994, 367.
- [28] A. Podshivalov, W. Clevenger, O. Matveev, B. Smith, J. Winefordner, *Applied Spectroscopy* 54 (2000) 175.
- [29] O. Matveev, N. Zorov, Y. Kuzyakov, *Journal of Analytical Chemistry* 34 (1979) 846.

- [30] O. Matveev, W. Clevenger, L. Mordoh, B. Smith, J. Winefordner, in Resonance Ionization Symposium Conference Proceedings, American Institute of Physics, 1996, 171.
- [31] D. Pappas, O. Matveev, B. Smith, M. Shepard, A. Podshivalov, J. Winefordner, *Applied Optics* 39 (2000) 4911.
- [32] Hamamatsu Corporation, Hamamatsu Product Catalog, New York (1996).
- [33] Princeton Instruments, Princeton Instruments Catalog, Trenton, NJ (1996).
- [34] U. Ellenberger, A. Glinz, J. Balmer, *Measurement Science and Technology* 4 (1993) 1430.
- [35] J. Ingle, S. Crouch, *Spectrochemical Analysis*, Prentice Hall, Upper Saddle River, New Jersey, 1988.
- [36] M. Grossman, R. Lagushenko, J. Maya, *Physical Review A* 34 (1986) 4094.
- [37] N. Omenetto, *Analytical Laser Spectroscopy*, John Wiley & Sons, New York, 1979.
- [38] *The Photonics Design and Applications Handbook*, Laurin Publishing Company, Pittsfield, MA, 1999.
- [39] A. Podshivalov, M. Shepard, O. Matveev, B. Smith, J. Winefordner, *Journal of Applied Physics* 86 (1999) 5337.
- [40] S. Kramer, J. Young, G. Hurst, M. Payne, *Optics Communications* 30 (1979) 47.
- [41] N. Karnov, B. Krynetzkii, O. Stel'makh, *Kvantovaya Elektronika* 4 (1977) 2275.
- [42] R. Ambartzumian, G. Bekov, V. Letokhov, V. Mishin, *Pis'ma Zhurnalu Eksperimental'noy i Teoreticheskoy Fiziki* 31 (1974) 595.
- [43] T. Ducas, M. Littaman, R. Freeman, D. Kleppner, *Physical Review Letters* 35 (1975) 366.
- [44] A. Smith, J. Goldsmith, D. Nitz, S. Smith, *Physical Review A* 22 (1980) 577.

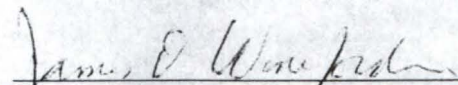
- [45] D. Beeman, T. Calcott, S. Kramer, F. Arakawa, G. Hurst, E. Nussbaum, *International Journal of Mass Spectrometry and Ion Physics* 34 (1980) 89.
- [46] Y. Kudriavtzev, V. Letokhov, V. Petrunin, *Pis'ma Zhurnalu Eksperimental'noy i Teoreticheskoy Fiziki* 42 (1985) 23.
- [47] U. Brinkman, W. Hartwig, H. Telle, H. Walther, *Applied Physics* 5 (1974) 109.
- [48] D. Bradley, C. Dudan, P. Ewart, A. Purdie, *Physical Review A* 13 (1976) 1416.
- [49] R. Ambartzumian, V. Letokhov, *Applied Optics* 11 (1972) 354.
- [50] R. Ambartzumian, V. Letokhov, E. Ryabov, N. Chekalin, *Pis'ma Zhurnalu Eksperimental'noy i Teoreticheskoy Fiziki* 20 (1974) 597.
- [51] R. Ambartzumian, V. Kalinin, V. Letokhov, *Pis'ma Zhurnalu Eksperimental'noy i Teoreticheskoy Fiziki* 13 (1971) 305.
- [52] G. Hurst, M. Nayfeh, J. Young, *Physical Review A* 15 (1977).
- [53] M. Zimmerman, T. Ducas, M. Littaman, D. Kleppner, *Journal of Physics B* 11 (1978) L11.
- [54] W. Cooke, T. Gallagher, *Physical Review Letters* 41 (1978) 1648.
- [55] M. Aymar, R. Champen, C. Deslart, J. Keller, *Journal of Physics B* 14 (1981) 4489.
- [56] A. Mizolek, *Journal of Analytical Chemistry* 53 (1981) 118.
- [57] P. Dyer, G. Baldwin, C. Kittrel, D. Imre, E. Abramson, *Applied Physics Letters* 42 (1983) 311.
- [58] D. Andrews, *Lasers in Chemistry*, Springer-Verlag, New York, 1997.
- [59] Oriel Instruments, *The Book of Photon Tools*, Oriel Instruments, Stratford, CT, 2001.
- [60] *Handbook of Optics*, Optical Society of America, McGraw-Hill, New York, 1978.

- [61] E. Saloman, *Spectrochimica Acta B* 43 (1991) 319.
- [62] M. Shepard, J. Temirov, O. Matveev, B. Smith, J. Winefordner, *Optics Communications*, in press (2002).
- [63] A. Podshivalov, W. Clevenger, O. Matveev, B. Smith, J. Winefordner, *Applied Spectroscopy* 54 (2000) 175.
- [64] P. Potts, *A Handbook of Silicate Rock Analysis*, Chapman & Hall, New York, 1987.
- [65] K. Kanaya, S. Okayama, *Journal of Physics D* 5 (1972) 43.
- [66] A. Jelalian, *Laser Radar Systems*, Artech House, Boston, 1992.
- [67] N. Parikh, J. Parikh, *Optics and Laser Technology* 34 (2002) 177.
- [68] K. Ogawa, *IEEE Transactions on Nuclear Science* 44 (1997) 1521.
- [69] T. Histen, O. Guell, I. Chavez, J. Holcombe, *Spectrochimica Acta B* 51 (1996) 1279.

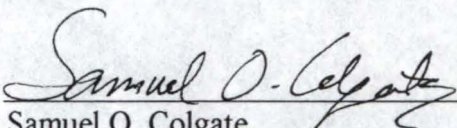
BIOGRAPHICAL SKETCH

Michael Shepard was born on September 23rd, 1974, in Asheville, North Carolina. He is the son of Deena Duncan and Charles Shepard. He lived most of his childhood in the mountains of western North Carolina and graduated from McDowell County High School in 1993. Michael then graduated from Western Carolina University in 1997 with a Bachelor of Science degree in chemistry. Michael attended graduate school at the University of Florida and completed his doctoral research in 2002 under the direction of Dr. James D. Winefordner.

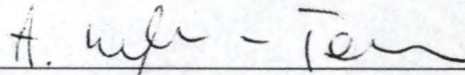
I certify that I have read this study and that in my opinion it conforms to acceptable standards of scholarly presentation and is fully adequate, in scope and quality, as a dissertation for the degree of Doctor of Philosophy.


James D. Winefordner, Chairman
Professor of Chemistry

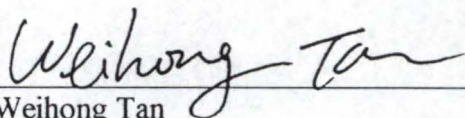
I certify that I have read this study and that in my opinion it conforms to acceptable standards of scholarly presentation and is fully adequate, in scope and quality, as a dissertation for the degree of Doctor of Philosophy.


Samuel O. Colgate
Professor of Chemistry

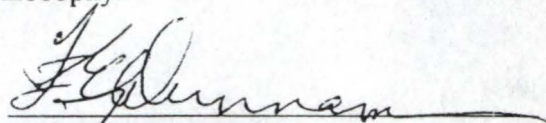
I certify that I have read this study and that in my opinion it conforms to acceptable standards of scholarly presentation and is fully adequate, in scope and quality, as a dissertation for the degree of Doctor of Philosophy.


Anna Brajter-Toth
Associate Professor of Chemistry

I certify that I have read this study and that in my opinion it conforms to acceptable standards of scholarly presentation and is fully adequate, in scope and quality, as a dissertation for the degree of Doctor of Philosophy.


Weihong Tan
Associate Professor of Chemistry

I certify that I have read this study and that in my opinion it conforms to acceptable standards of scholarly presentation and is fully adequate, in scope and quality, as a dissertation for the degree of Doctor of Philosophy.



F. Eugene Dunnam
Professor of Physics and Astronomy

This dissertation was submitted to the Graduate Faculty of the Department of Chemistry in the College of Liberal Arts and Sciences and to the Graduate School and was accepted as partial fulfillment of the requirements for the degree of Doctor of Philosophy.

August 2002

Dean, Graduate School

LD
1780
20 02

.5547

UNIVERSITY OF FLORIDA

3 1262 08555 3559